CHARACTERISTICS OF A MARINE STRATOCUMULUS TO CUMULUS CLOUD TRANSITION

A Thesis

by

ALLISON LAUREN ZAPALAC

Submitted to the Office of Graduate and Professional Studies of
Texas A&M University
in partial fulfillment of the requirements for the degree of

MASTER OF SCIENCE

Chair of Committee,	Anita D. Rapp
Committee Members,	Courtney Schumacher
	Deborah J. Thomas
Head of Department,	Ping Yang

December 2014

Major Subject: Atmospheric Sciences

ABSTRACT

The studies in this thesis aim to improve the overall understanding of the characteristics of the marine stratocumulus to shallow cumulus transition over the southeast Pacific Ocean. This study uses observations from CloudSat and CALIPSO satellite instruments in NASA's A-Train constellation to analyze environmental, microphysical and macrophysical cloud properties, precipitation, and cloud radiative effects along the climatological wind trajectories between January 2007 and December 2010. The interannual, intraseasonal, and diurnal variability of clouds across the transition over the study region is also examined.

Results show that as trade winds advect equatorward from the Peruvian coastline to warmer waters, thick, persistent, low-level stratocumulus clouds with high cloud fractions and strong shortwave cloud radiative effects in the southern portion of the study region gradually transition to shallow cumulus clouds with decreased cloud fractions and cloud radiative effects. The speed of this transition exhibits interannual, seasonal, and diurnal differences associated with changes in the large-scale environment. More frequent and intense precipitation along the trajectory corresponds to a more rapid reduction in cloud cover, implying that it may play a role in the transition through its reduction in cloud water and stabilizing effect on the boundary layer. Results also suggest that capturing the variability in the transition from stratocumulus to shallow cumulus clouds is important for improving representation of cloud feedback effects in current climate models.

ACKNOWLEDGEMENTS

I would like to express my sincere gratitude to my advisor, Dr. Anita Rapp, for her continued support, ideas, guidance, and patience throughout my work on this project. Words cannot express how much I appreciate the time and effort she has given me throughout my graduate studies, and for giving me the opportunity to continue my education. I would also like to thank my committee members Dr. Courtney Schumacher and Dr. Deborah Thomas for their guidance, support, and constructive feedback of my work throughout the course of this research.

Thanks also go to my friends and colleagues and the department faculty and staff for making my time at Texas A&M University a great experience. I also want to extend my gratitude to the National Science Foundation as this research would not have been possible without their support through the grant AGS-1128024.

Finally, I could not have done this without the patience, love and support of my husband Joshua, and to my amazing family for their encouragement, support, and unconditional love. I would not be where I am today without their unfailing love and support.

TABLE OF CONTENTS

Page

ABSTRACT ii

ACKNOWLEDGEMENTS iii

TABLE OF CONTENTS iv

LIST OF FIGURES vi

LIST OF TABLES x

1. INTRODUCTION 1

- 1.1 Overview of clouds in the subtropical ocean 1
- 1.2 Overview of stratocumulus to cumulus transition 4
- 1.3 The southeast Pacific stratocumulus region 12
- 1.4 Main goals of thesis 16

2. METHODOLOGY 17

- 2.1 Data 17
- 2.2 Methods 24

3. RESULTS 34

- 3.1 Climatological representation 34
- 3.2 Interannual variability 45
- 3.3 Seasonal variability 55
- 3.4 Diurnal variability 65

4. SUMMARY AND DISCUSSION 72

- 4.1 Summary 72
- 4.2 Discussion 75
- 4.3 Limitations 79
- 4.4 Future work 80

5. CONCLUSIONS 81

REFERENCES 82

LIST OF FIGURES

FIGURE Page

1 Illustration of processes important for stratocumulus formation and development within the boundary layer.(Figure from Wood 2012).....3

2 Schematic showing structure of marine stratocumulus in (a) the shallow, well-mixed boundary layer and (b) deeper, cumulus-coupled boundary layers. The gray arrows indicate the primary motions on the boundary layer scale, while smaller red arrows indicate the small scale entrainment mixing taking place at the inversion atop the layer. (Figure from Wood 2012) 6

3 GOES visible satellite images. (a) Open-cell mesoscale cellular convection 1445 UTC on October 18th and (b) closed cellular convection at 1445 UTC October 16th. The open-cellular structures are roughly 30 km across (Comstock et al. 2005), whereas the cloudy portions of open cells are about 10 km (Wood and Hartmann 2004). (Figure from Comstock et al. 2005) 9

4 Illustration of key mechanisms that allow stratocumulus to form in the southeast Pacific Ocean for the VOCALS field campaign. (Figure from Wood et al. 2011) 13

5 Cloud fraction on the third day of the selected trajectories, and medians of the forward (white line) and the backward (black line) climatological trajectories in the southeast Pacific and Atlantic Oceans. (Sandu et al. 2010) 31

6 Trajectory coordinate points (*) with the 2°x 2° boxes around each of the trajectory data points (*).The other points (+) are trajectory points calculated from the Appendix of Sandu et al. (2010) 31

7 Four-year mean representation of the environmental variables (a) SST in °C(b) temperature profile (K), (c) the LTS (K), and (d) specific humidity (g kg-1), along the climatological wind trajectory in the southeast Pacific 35

8 Four-year mean representation of each cloud variable observed along the climatological wind trajectory in the southeast Pacific. The panels are (a) cloud fraction (%), (b) cloud layer top and base heights (m), (c) optical depthduring the day (unitless), (d) effective radius during the day (microns), (e) non-precipitating cloud liquid water path (g m-2), and (f) total low cloud fraction (in %).....38

FIGURE Page

9 Four-year mean for (a) the rain frequency (% likelihood) and (b) the rain rate (mm d-1) for all cloud observations .The red and blue lines in figure 8(a) represent the likelihood that rain is present at the surface over all observations (blue) and the likelihood that rain is certain at the surface over all observations (red). The rain rate in Figure 8(b) is separated by the conditional (blue) rain rate and the unconditional (red) rain rate (mm d-1) 41

10 Four-year mean along the climatological wind trajectory in the southeast Pacific for (a) longwave cloud top cooling (K d-1), (b) shortwave cloud top heating (K d-1), and (c) top of atmosphere shortwave cloud radiative effect (Wm-2).....44

11 The sea surface temperature (°C) along the climatological wind trajectoryin the southeast Pacific for each year relative to the 4-year mean(black dashed) ..46

12 The temperature profile (K) along the climatological wind trajectory in the southeast Pacific for 2007-2010. 47

13 The LTS (K) for each year relative to the 4-year mean climatology(black dashed) 48

14 The specific humidity (g kg-1) along the climatological wind trajectory in the southeast Pacific for 2007-2010 49

15 The cloud fraction (%) along the climatological wind trajectory in the southeast Pacific for (a) 2007, (b) 2008, (c) 2009, and (d) 2010.....51

16 Cloud layer top and base heights (m) along the climatological wind trajectory in the southeast Pacific for 2007.....52

17 The LWP (g m-2) for each year relative to the 4-year mean (black dashed) along the climatological wind trajectory in the southeast Pacific 53

18 The rain possible frequency (% likelihood) and conditional rain rate (mm day-1) for cloud observations for each year relative to the 4-year meanclimatology (black dashed) 54

19 The longwave cooling rate (K d -1) at the cloud top for each year relative to the 4-year mean climatology (black dashed) 55

FIGURE Page

20 The SST (°C) along the climatological wind trajectory in the southeast Pacific for each season relative to the 4-year mean (black dashed) 57

21 The temperature profile (K) along the climatological wind trajectory in the southeast Pacific for both (a) MAM and (b) SON.....57

22 The LTS (K) along the climatological wind trajectory in the southeast Pacific for each season relative to the 4-year mean (black dashed.....58

23 The specific humidity profile (g kg-1) along the climatological wind trajectory in the southeast Pacific for both (a) MAM and (b) SON 58

24 Cloud fraction (%) along the climatological wind trajectory in the southeast Pacific for (a) DJF, (b) MAM, (c) JJA, and (d) SON.....60

25 Cloud layer top and base height (m) along the climatological wind trajectory in the southeast Pacific for (A) MAM and (B) SON 60

26 The LWP (g m-2) for each season relative to the 4-year mean climatology (black dashed) 61

27 (a) The rain possible frequency (% likelihood) and (b) the conditional rain rate (mm day-1) of cloud observations for each season relative to the 4-year mean climatology (black dashed) 62

28 The TOA shortwave cloud radiative effect (W m-2) for each season relative to the 4-year mean climatology (black dashed).....63

29 The longwave cloud top cooling rate (K d-1) for each season compared to the 4-year mean climatology (black dashed) 64

30 The temperature profiles (K) for (A) day and (B) night.....66

31 The cloud fraction (%) along the climatological wind trajectory in the southeast Pacific for (A) daytime overpasses and (B) nighttime overpasses 67

32 The cloud layer top and base heights (m) for day (pink) and night (blue) 67

33 The LWP (g m-2) for day (pink) and night (blue).....68

FIGURE Page

34 The rain possible frequency (blue) and the rain certain frequency (red)for (A) day and (B) night 69

35 The conditional rain rates (mm d-1) for (A) day and (B) night.....69

36 The longwave cloud top cooling (K d-1) for day (pink) and night (blue) 70

LIST OF TABLES

TABLE Page

1 Data products and variables used in research from 2007-2010 20

2 List of coordinate points used in study and the total number of observations collected within each 2°x 2° box around each coordinate 32

1. INTRODUCTION

1.1 Overview of clouds in the subtropical ocean

Clouds cover nearly two thirds of Earth's surface and have a significant impact on Earth's climate through their influence on the radiation budget (Stephens et al. 1981; Ramanathan et al. 1989; Stubenrauch et al. 2010). High clouds both reflect incoming solar radiation and absorb outgoing thermal radiation emitted by the surface, generally leading to a warming effect of the atmosphere (Hartmann et al. 1992; Klein and Hartmann 1993; Kollias et al. 2004). Conversely, low clouds reduce the amount of incoming solar energy reaching the surface by reflecting sunlight back to space and absorb and emit nearly the same amount of longwave radiation as the surface (Hartmann et al. 1992), resulting in a cooling effect of the surface (Schneider 1972; Kollias et al. 2004). Over the subtropical oceans, low, optically thick stratocumulus clouds with their limited vertical extent (cloud top heights rarely exceed 2 km), long-lasting, widespread coverage and their high albedo that reflects large amounts of incoming solar radiation, produce a strong cooling effect on earth's climate.

Some of the largest uncertainties in the projections of future climate arise from the representation of clouds in climate models (Stephens 2005; Soden and Held 2006; Dufresne and Bony 2008), particularly in the representation of the physics of shallow clouds (Bony and Dufresne 2005; Webb et al. 2006). Because they cover vast areas of earth's surface and are highly reflective to shortwave radiation, marine stratocumulus clouds have a significant impact on the climate system making them an important

component of radiation balance (Muhlbauer et al. 2014). They also contribute to the water cycle by transporting moisture from the surface to the free troposphere. Understanding the physics of marine stratocumulus clouds is important for improving estimates of future climate prediction (Klein and Hartmann 1993; Stephens 2005; Teixeira et al. 2011). In particular, the parameterization of stratocumulus clouds in the marine boundary layer is a significant source of uncertainty in climate predictions (Bony and Dufresne 2005; Chung and Teixeira 2012). The complicated physical processes associated with the transition from marine stratocumulus to shallow cumulus clouds are particularly challenging to understand and predict, which is one of the reasons why the uncertainty is so large in global weather and climate models (Teixeira et al. 2011; Cheng and Xu 2013).

Marine stratocumulus clouds typically form on the eastern basins of the subtropical Atlantic and Pacific Oceans beneath a strong capping inversion that is associated with the descending branch of the Hadley cell where sinking motion occurs (Klein and Hartmann 1993, 1994). Extensive areas of stratocumulus clouds are commonly observed as either solid or broken cloud decks in regions where warm, subsiding air is present over cooler sea surface temperatures (SSTs) (Klein and Hartmann 1993; Wood 2012). The strong subsidence helps to maintain the necessary temperature inversion, which keeps the boundary layer shallow and well mixed (Xu et al. 2004; Richter and Mechoso 2004, 2006; Wood 2012).

Figure 1 from Wood (2012) illustrates the general structure of stratocumulus clouds in the boundary layer and indicates the role of key processes such as radiative

heating and cooling, latent heating, surface fluxes, and entrainment within the cloud layer that impact the development and maintenance of stratocumulus clouds. Strong longwave radiative cooling at the cloud top drives the instability within the stratocumulus cloud layer (Lilly 1968; Wood 2012). During the day, the absorption of solar radiation heats up the cloud layer and reduces the longwave radiative cooling and instability within the cloud layer, which leads to the gradual thinning and breakup of the stratocumulus cloud layer. During the overnight hours, the longwave radiative cooling increases, resulting in increased instability, stronger turbulence within the cloud, and more efficient cloud coupling with the surface moisture supply (Turton and Nicholls 1987; Rogers and Koracin 1992; Wood 2012). Therefore, the maximum stratocumulus cloud coverage occurs in the early morning hours before sunrise (Duynkerke et al. 2004; Wood 2012).

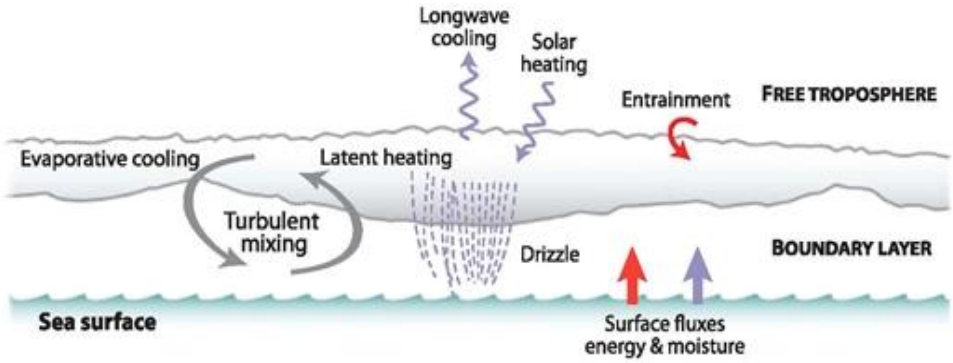

Figure 1: Illustration of processes important for stratocumulus formation and development within the boundary layer. (Figure from Wood 2012)

Latent heating released in the upward branches of the convective elements and evaporative cooling found in the downdrafts adds an additional source of turbulence to strengthen the convection (Moeng et al. 1992; Wood 2012). The turbulent mixing within the cloud layer controls the development of mesoscale organization and also frequently couples the cloud layer to the moisture source found at the surface (Nicholls 1984; Shao and Randall 1996). Both turbulent eddies and evaporative cooling drive entrainment at the top of the stratocumulus-topped boundary layer, which allows the marine boundary layer to deepen over time (Wood 2012). The surface latent heat flux, which is controlled by the relative humidity, temperature, and wind speed at the surface, provides the main source of moisture for the stratocumulus-topped boundary layer (Wood 2012).

1.2 Overview of stratocumulus to cumulus transition

As the trade winds advect air toward the equator over the warmer sea surface, the boundary layer warms and deepens (Krueger et al. 1995; Wyant et al. 1997; Wood 2012). Several studies have documented the changes in cloud structure of stratocumulus clouds as they advect equatorward (Albrecht et al. 1995, Bretherton and Wyant 1997). The Atlantic Stratocumulus Transition Experiment (ASTEX), conducted during June of 1992 in the northeast Atlantic, investigated the mechanisms and processes responsible for the uniform shallow stratocumulus to trade wind cumulus transition and showed that the processes involved in the decoupling of the surface and cloud layer were important for the stratocumulus to cumulus transition offshore (Albrecht et al. 1995). An increase

in convective activity over the warmer waters strengthened the turbulence within the boundary layer, leading to an enhancement of entrainment near the cloud tops (Bretherton and Wyant 1997; Sandu et al. 2010). This enhanced entrainment helps to stabilize the stratocumulus cloud layer, therefore decoupling the cloud layer from the surface and inhibiting surface moisture from reaching the cloud layer. As this occurs, the environment near the surface is conditionally unstable and moisture is readily available, allowing shallow cumulus clouds to form underneath the stable cloud deck (Albrecht et al. 1995; Wang and Lenschow 1995; Sandu et al. 2010). As the developing cumulus clouds deepen, they recouple the stratocumulus cloud layer with the surface (Sandu et al. 2010). As the updrafts from the developing shallow cumulus clouds become vigorous enough to penetrate the inversion, they entrain warm dry air from above the boundary layer (Wang and Lenschow 1995; Bretherton and Wyant 1997). This weakens the temperature inversion and begins to thin and evaporate the stratocumulus deck until it breaks up into thin broken patches, leaving only shallow cumulus clouds (de Szoeke et al. 2006). By deepening the boundary layer and evaporating the stratocumulus cloud layer, shallow cumulus clouds help bring about the transition from stratocumulus to shallow cumulus clouds (Albrecht et al. 1995), causing cloudiness to decrease (de Szoeke et al. 2006). According to Sandu et al. (2010), this transition from stratocumulus to shallow cumulus clouds takes about 3 days. An overview of this transition is illustrated in Figure 2 with the top panel representing a shallow, well mixed layer and the bottom panel representing a decoupled boundary layer.

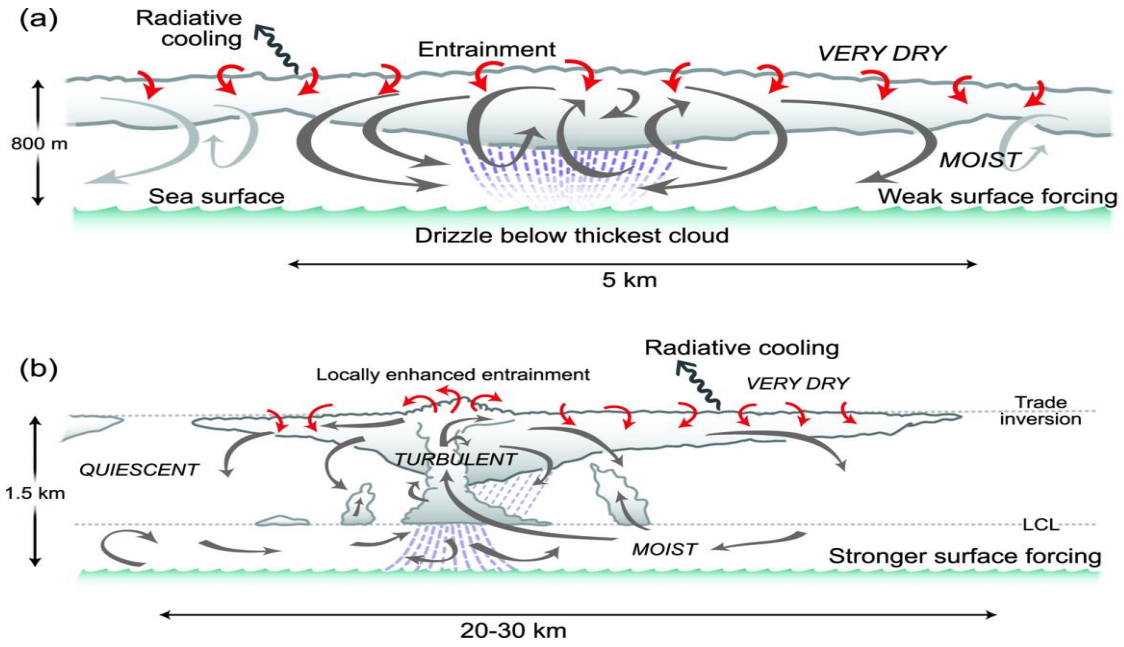

Figure 2: Schematic showing structure of marine stratocumulus in (a) the shallow, well-mixed boundary layer and (b) deeper, cumulus-coupled boundary layers. The gray arrows indicate the primary motions on the boundary layer scale, while smaller red arrows indicate the small scale entrainment mixing taking place at the inversion atop the layer. Figure from Wood (2012).

In October - November 2008, the VAMOS Ocean-Cloud-Atmosphere-Land Study Regional Experiment (VOCALS-REx) studied boundary layer clouds on a transect along 20° S in the southeast Pacific Ocean (Bretherton et al. 2010). Bretherton et al. (2010) found that further offshore, the free tropospheric air was cooler and drier than along the coast, which weakened the inversion and further enhanced longwave cooling at the top of the cloud layer, thus allowing turbulence to strengthen within the cloud layer. This led to stronger entrainment and a deeper boundary layer further offshore (Bretherton et al. 2010). As the boundary layer deepened along the 20°S

transect, it created more variability in the liquid water path (LWP) and decoupled the vertical structure in the marine boundary layer, which allowed stratocumulus clouds further offshore to exhibit stronger organization, higher liquid water paths, and extensive drizzle (Bretherton et al. 2010).

Marine stratocumulus clouds frequently produce light precipitation, with drizzle as the most common form observed (Nicholls and Leighton 1986; Petty 1995; Austin et al. 1995; Wood 2005), as illustrated in Figure 1 (Wood 2012). A number of field experiments have studied the formation and frequency of drizzle in stratocumulus clouds and its impact on the marine boundary layer (Austin et al. 1995; Stevens et al. 2003; Comstock et al. 2005). As previously mentioned, the longwave cooling at night helps to thicken the stratocumulus clouds, increasing the likelihood for precipitation to occur in the early morning hours. The formation of precipitation allows latent heat to be released and also removes water from the cloud layer, thus heating, stabilizing, and drying the cloud layer. Therefore, studies (Austin et al. 1995; Stevens et al. 2003; Comstock et al. 2005) have found that precipitation depletes both the cloud amount and cloud liquid water path and that the drizzling regime corresponds to increased variability of the properties that make up the cloud and boundary layer (Comstock et al. 2005). The evaporation of drizzle helps to cool and moisten the subcloud region, which contributes to stabilizing the boundary layer (Comstock et al. 2005). Simulations from Comstock et al. (2005) indicate that the evaporation of drizzle inhibits the heat and moisture flux beneath the nocturnal stratocumulus cloud layer. These conditions, like the strong drizzle events observed during the ASTEX campaign in the northeast Atlantic, are frequently

observed with patchy cloud conditions (Stevens et al. 1998) and suggest that open-celled cloud patterns correspond to heavy drizzle (Stevens et al. 2005).

Recent studies have focused on better understanding the role of precipitation in the transition from stratocumulus to shallow cumulus (Bretherton et al. 2004, 2010; vanZanten and Stevens 2005). There is evidence that precipitation may actually speed up the stratocumulus to shallow cumulus transition process (vanZanten and Stephens 2005). During Dynamics and Chemistry of Marine Stratocumulus II (DYCOMS-II), vanZanten and Stevens (2005) showed that localized patches of enhanced precipitation corresponded with regions of open cellular convection (pockets of open cells) off the California coast. Pockets of open cells (POCs) are regions of open-cellular cloud structures surrounded by or adjacent to regions of closed-cellular cloud fields (Stevens et al. 2005). Figure 3 from Comstock et al. (2005) illustrates the differences in the boundary layer between an (a) open-cell and (b) closed cell mesoscale cellular convection in GOES visible satellite images. The closed cell structures often have surface convergence and updrafts where higher levels of moisture are present, which contribute to the replenishment of moisture into the cloud (Comstock et al. 2005). A POC sampled by airborne radar during the DYCOMS-II campaign (Stevens et al. 2003) showed that the POC region was comprised of mesoscale cells with enhanced convection near the edges of the domain where locally higher cloud top heights and enhanced reflectivity that reached the surface (drizzle) were observed (Stevens et al. 2005). Stevens et al. (2005) also found that the interiors of these mesoscale cellular walls showed lower cloud top heights and even had regions of clearing, or low cloud fraction.

The study concluded that the observed high drizzle rates could likely stabilize the boundary layer, allowing shallow cumuli to develop and instigate a transition within the cloud structure (vanZanten and Stevens 2005; Stevens et al. 1998, 2005).

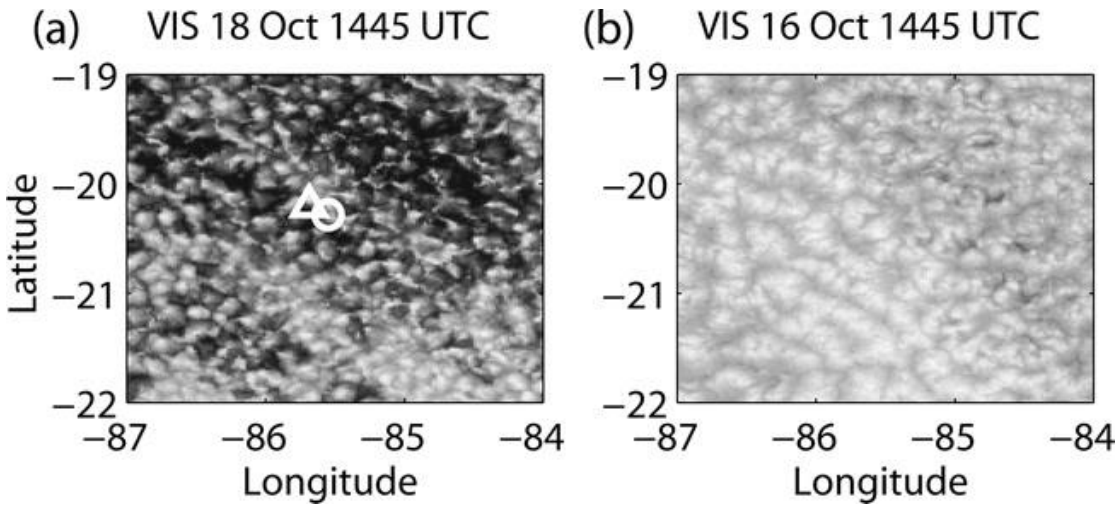

Figure 3: GOES visible satellite images. (a) Open-cell mesoscale cellular convection 1445 UTC on October 18th and (b) closed cellular convection at 1445 UTC October 16th. The open-cellular structures are roughly 30 km across (Comstock et al. 2005), whereas the cloudy portions of open cells are about 10 km (Wood and Hartmann 2004). (Figure from Comstock et al. 2005)

Bretherton et al. (2004) observed drizzle when thick clouds were present in the overnight and early morning hours during a 2 week cruise in September of 2001 as part of East Pacific Investigation of Climate (EPIC). They concluded that the entrainment of dry air played a major role in influencing the thickness of stratocumulus clouds, but light drizzle could also reduce the amount of turbulence within the cloud. A POC was observed during this field experiment as a boundary between open and closed cellular convection passed over one of the research vessels. The shipborne radar measured

frequent periods of higher reflectivity (a proxy for drizzle, e.g., Vali et al. 1998) that extended down to the surface (Stevens et al. 2005) when the region of open cells passed over.

The stratocumulus to shallow cumulus transition has been researched using several approaches, such as large-scale statistical studies (Klein and Hartmann 1993; Wood and Hartmann 2006), observational studies in a specific region (Bretherton et al. 2004, 2010; vanZanten and Stevens 2005), mixed layer modeling studies (Bretherton and Wyant 1997), and high resolution simulations (Krueger et al. 1995; Wyant et al. 1997), with each approach providing crucial information about the transition processes (Chung et al. 2012).

In a recent study, Sandu et al. (2010) performed an analysis of satellite observations and meteorological reanalysis along Lagrangian wind trajectories in stratocumulus to cumulus transitions. They composited thousands of individual Lagrangian trajectories over four subtropical regions within the Atlantic and Pacific Oceans where stratocumulus clouds are commonly observed and compared these trajectories to the climatological trajectories computed from the mean five-year wind field. After comparing the observations along the climatological and the individual trajectories, they concluded that the climatological trajectories are highly representative of the mean of the individual trajectories, partially due to the steady features found in the trade winds (Riehl et al. 1951, Sandu et al. 2010). Therefore, the climatological trajectories can be used to represent the mean 3-day transition in clouds along the trajectory in the Southeast Pacific. Sandu et al. (2010) concluded that the transition,

which is characterized primarily by a decrease in cloud fraction, is mainly correlated with an increase in SSTs. Their study primarily focused on the changes in cloud fraction along the trajectories across the stratocumulus to shallow cumulus transition, rather than on the properties of the clouds or other factors, such as precipitation, that may be important in this transition. Since the climatological trajectories were highly representative of the 3-day transition from stratocumulus to cumulus, this analysis will use the climatological trajectories from Sandu et al. (2010) to study the cloud structure and radiative impacts across the transition in further detail.

This type of analysis has been previously applied by Teixeira et al. (2011) to evaluate weather and climate models along a cross section in the northeastern Pacific Ocean, from stratocumulus clouds situated off the coast of California across the trade winds where shallow convection dominates, to the ITCZ region where deep convection is prominent. Teixeira et al. (2011) showed that many of the weather and climate prediction models underestimated the amount of clouds in the stratocumulus regime, both in cloud cover and in liquid water path. They suggested that these underestimates occurred due to the timing of the transitions, as the transitions occurred too early in models compared to the observations (Teixeira et al. 2011; van der Dussen et al. 2013). They also found a large spread between models estimates of transitions in cloud cover, liquid water path, and shortwave radiation. While Teixeira et al. (2011) analyzed the cross-section of precipitation across the transition in the northeastern Pacific, the measurements they used are not sensitive enough to the light precipitation that is most prevalent across the transition from stratocumulus to shallow cumulus. This study will

apply a similar analysis technique along the Sandu et al. (2010) trajectories with satellite data over the southeast Pacific for a much longer period.

1.3 The southeast Pacific stratocumulus region

The interactions between the western portion of the South American continent and the Southeast Pacific (SEP) Ocean are important for both the regional and global climate system (Wood et al. 2011). Figure 4 from Wood et al. (2011) provides an illustration of the mechanisms important for the stratocumulus cloud layer to form in this region. The Andes Cordillera (the longest mountain chain in the world), form a sharp barrier to zonal flow, resulting in strong winds (coastal jet) that flow parallel to the coasts of Chile and Peru (Garreaud and Muñoz 2004). There is also large-scale subsidence that occurs year-round over the southeastern Pacific Ocean, resulting in a quasi-permanent surface anticyclone that is centered roughly at 27°S, 90°W (Garreaud and Muñoz 2004). This subtropical high brings southern low-level winds along the coastline of Chile and Peru, which drives the strong oceanic upwelling along the coasts of Chile and Peru, bringing cold, deep, nutrient-rich waters up to the surface (Garreaud and Muñoz 2004, Wood et al. 2011). As a result, a tongue of cold surface water is found along the west coast of South America where the coastal sea-surface temperatures are colder along the Chilean and Peruvian coasts than at any comparable latitude elsewhere (Wood et al. 2011). Both the cold ocean surface and the warm, dry air aloft due to subsidence are ideal for the formation of marine stratocumulus clouds, and help to support the largest and most persistent subtropical stratocumulus deck in the world in

this region (Klein and Hartmann 1993, Bretherton et al. 2004, 2010). The subsidence that drives the development of stratocumulus is seasonally influenced by the downward branch of the Hadley cell, where a region of subsidence is located at 30°S (Liang and Evans 2011) and also influenced by location of the Walker circulation in the Pacific Ocean, which is an east-west circulation with rising air in the west Pacific and sinking air over the east Pacific Ocean (rather than the north-south circulation associated with the Hadley cell) (Liang and Evans 2011).

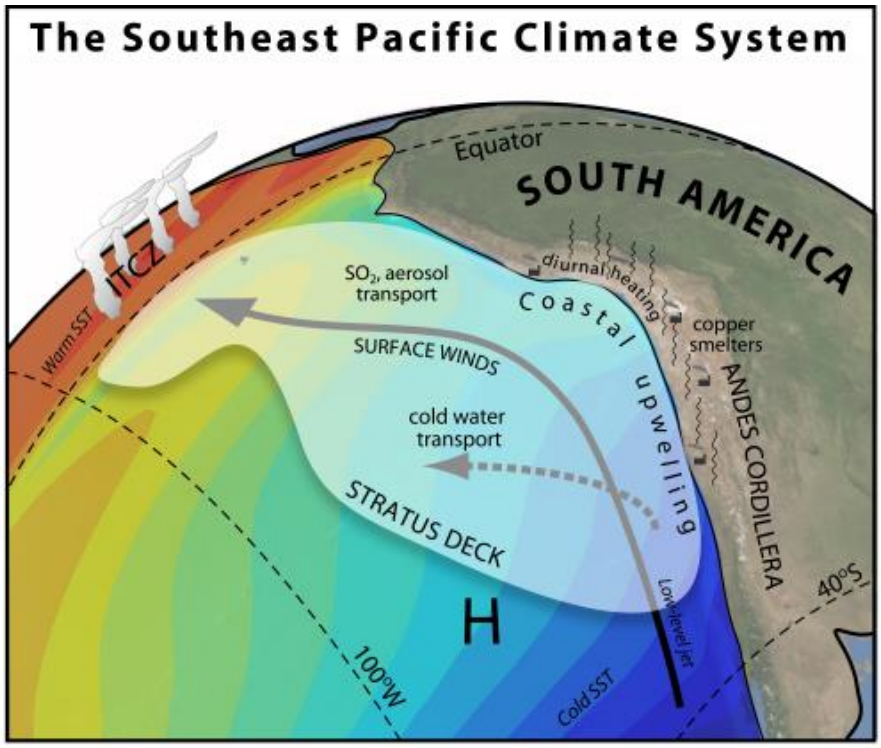

Figure 4: Illustration of key mechanisms that allow stratocumulus to form in the southeast Pacific Ocean for the VOCALS field campaign. (Figure from Wood et al. 2011)

The presence of this expansive and persistent cloud deck has a major impact on earth's radiation budget, mainly due to high amount of reflected solar radiation, which acts to cool to surface below, resulting in a stronger inversion and tighter couplings between the upper ocean and the lower atmosphere. It is also likely that the transition from stratocumulus to shallow cumulus clouds in this region plays a significant role in cloud-climate feedbacks, which is one of the reasons why it is important to better understand the factors that control this transition (Teixeira et al. 2011; Chung et al. 2012).

Although a number of field experiments have improved the understanding of stratocumulus clouds in the southeast Pacific (Bretherton et al. 1992, 2004; Austin et al. 1995; Wyant and Bretherton 1997), there remains a lack of spatial and temporal coverage of marine stratocumulus cloud studies over the southeast Pacific Ocean because field experiments typically last for only a few months and are limited to a small region due to instrumentation and costs. This study will therefore address some of the spatial and temporal coverage issues with the use of new satellite measurements.

While past studies have used satellite data to investigate clouds in this region, they had inherent limitations. Past studies have used Moderate Resolution Imaging Spectroadiometer (MODIS) data to study the properties of these clouds, but it only performs retrievals during the daytime, which is a limitation when analyzing stratocumulus clouds since there is a large diurnal cycle in their characteristics. Another issue is the lack of sensitivity to detect drizzle in the low level clouds with traditional spaceborne sensors. Past studies have used satellite passive microwave instrumentation

to look at precipitation estimates (Wilheit 1986; Kummerow et al. 2001); however, the lack of sensitivity to light precipitation limits the ability to observe drizzle in low-lying clouds like shallow cumulus and stratocumulus (Rapp et al. 2013). Jensen et al. (2008) attempted to indirectly detect drizzling scenes by using a 15 μm threshold in cloud effective radius data from the Moderate Resolution Imaging Spectroadiometer (MODIS); however, a recent study by Lebsock et al. (2008) showed that the effective radius threshold for precipitation is dependent on aerosol concentrations. In addition, precipitation in stratocumulus clouds peaks at night (Miller et al. 1998; Rapp et al. 2013) when cloud properties for visible/near-infrared sensors like MODIS are not available.

The recent launch of CloudSat's cloud profiling radar in 2006 allows us to overcome some of these issues. The 94 GHz radar onboard CloudSat provides a greater sensitivity than other spacebourne sensors to smaller cloud and precipitation droplets that are associated with drizzle (Rapp et al. 2013). In addition to CloudSat, the Cloud-Aerosol Lidar with Orthogonal Polarization (CALIOP) on CALIPSO was also launched in 2006 as part of NASA's A-Train constellation and was designed to provide better sampling of the vertical profiles of both aerosols and clouds (Winker et al. 2003). Data from four years of CloudSat and CALIPSO measurements will be used to not only improve the temporal and spatial sampling over the southeast Pacific Ocean, but also further our understanding of cloud and precipitation properties across the stratocumulus to shallow cumulus cloud transition in this region.

1.4 Main goals of thesis

This thesis focuses on analyzing the characteristics of marine stratocumulus clouds in the southeast Pacific Ocean as they transition to shallow cumulus clouds. A combination of retrieved cloud and environmental variables from NASA's A-Train constellation and reanalysis data are analyzed to examine the structure and properties of these clouds.

A better understanding of the cloud behavior in this transition region may help modelers improve the representation of low clouds and their radiative effects in global climate models. The primary focus of this study will be centered on three questions:

(1) What are the main cloud microphysical and macrophysical characteristics of marine stratocumulus clouds and shallow cumulus clouds across the transition region?

(2) How does precipitation vary across the transition from stratocumulus to shallow cumulus?

(3) How do the cloud radiative characteristics evolve with the cloud properties throughout the transition?

2. METHODOLOGY

2.1 Data

To better understand the transition from stratocumulus to cumulus clouds in the southeast Pacific Ocean, it is ideal to collect a plethora of measurements over an expansive region for an extended period of time. Past field campaigns have sampled stratocumulus in this region (Bretherton et al. 2004, 2010; Kollias et al. 2004); however, these campaigns have limited spatial and temporal coverage and only sample small areas with ships or aircraft over a couple of months. Other past studies that relied on passive satellite instruments like MODIS also faced limitations because of the difficulty of distinguishing between overlapping cloud structures (Morcrette and Fouquart 1985; Barker et al. 2008) and detecting drizzle in low-level clouds (Wilheit 1986; Kummerow et al. 2001). Even the Ku-band precipitation radar (PR) onboard the Tropical Rainfall Measuring Mission (TRMM) has limitations in measuring drizzle because of the PR's lack of sensitivity to small droplets (Schumacher and Houze 2000; Rapp et al. 2013).

To overcome some of these aforementioned issues, new observations will be used from several different instruments onboard satellites in NASA's Earth Observing System Afternoon satellite constellation, or A-Train, which include: the Cloud Profiling Radar (CPR) on CloudSat, and the Cloud-Aerosol Lidar with Orthogonal Polarization (CALIOP) on CALIPSO. The close alignment of the satellites that make up NASA's A-Train allows several different measurement methods to collect nearly simultaneous measurements of Earth's atmosphere (Stephens et al. 2008).

Launched in 2006, NASA's CloudSat carries a 94-GHz, near nadir-pointing, cloud profiling radar (CPR) that is sensitive to both cloud-size and precipitation-size particles (Stephens et al. 2002). The CPR is capable of penetrating through thin ice clouds at higher altitudes, allowing the radar to detect underlying, thicker clouds near the surface. The CPR has a footprint that is approximately 1.7 km along-track and 1.4 km across-track (Stephens et al. 2002). The vertical resolution of the CPR is 480 m and has a minimal detectable signal of -30 to -31 dBz (Haynes and Stephens 2007; Tanelli et al. 2008). Oversampling reduces the sample distance (Kim et al. 2007), allowing the CPR to measure about 125 vertical samples per profile, or one sample for every 240m, making it much more effective and useful to observe boundary layer clouds (Stephens et al. 2008). CloudSat orbits the Earth an average of fourteen times per day, with an equator crossing time of 0130 and 1330 UTC (Stephens et al. 2008). Unfortunately, low clouds with cloud top heights below ~1km may be underrepresented in CloudSat data because the two to three lowest samples, or bins, above the surface suffer from ground clutter contamination (Tanelli et al. 2008). However, CloudSat can detect the signals of heavy drizzle as low as 480 m and moderate drizzle at 720 m (2B-GEOPROF R04 quality statement http://www.cloudsat.cira.colostate.edu/dataICDlist.php?go=list&path =/2B-GEOPROF), which still renders it useful in the southeast Pacific since most precipitating clouds have tops greater than 720 m.

The horizontal and vertical resolution of data collected by CALIPSO's CALIOP is higher than that of CloudSat and has limited ground clutter near the surface, which is one of the reasons a combined CloudSat-CALIPSO data product is used in this study to

identify clouds. The active, dual-wavelength CALIOP instrument onboard CALIPSO is a laser operating at both 1084 nm and 532 nm with a spatial resolution of 30 meters vertically and 333m in the horizontal (Winker et al. 2003, 2007). The lidar is designed to provide information on the vertical profiles of both aerosols and clouds and distinguish the two (Winker et al. 2003, 2007). One limitation of the lidar is that thick clouds will fully attenuate the lidar; however, in these cases the CPR may be used for cloud detection. On the other hand, McGill et al. (2007) estimates that CALIPSO's lidar can detect very thin clouds with optical depths of 0.01 or smaller, which is far less than the detection limit of the CPR. Therefore, with the combination of observations from CloudSat's CPR and CALIPSO's lidar, this study uses a dataset that can penetrate optically thick cloud layers, detect optically thin layers, and therefore, presents a more complete representation of the vertical structure of clouds (Luo et al. 2009).

As stated previously, measurements from several CloudSat and CALIPSO data products are used to characterize the clouds in the southeast Pacific region. A number of different cloud properties are analyzed here including the vertical profile of cloud fraction, cloud top and base heights, particle effective radius, liquid water path, and optical depth. The precipitation frequency and rate is also examined to study the impacts of drizzle. Other derived products like upwelling and downwelling fluxes, radiative heating rates, and the cloud radiative effect at the top of the atmosphere are analyzed. Properties, such as temperature and moisture profiles, sea surface temperature, and lower tropospheric stability are used to characterize the environment. The CloudSat data products used in this analysis are listed in Table 1.

Products	Variables
2B-GEOPROF-LIDAR	Cloud layers, Cloud base height, Cloud top height
2B-CWC-RVOD	Liquid water path, liquid water content
2C-PRECIP-COLUMN	Rain certainty flag, SST, surface type
2C-RAIN-PROFILE	Rain rate
2B-FLXHR-LIDAR	Upwelling fluxes, downwelling fluxes, cloud radiative effect (TOA & surface), heating rates
2B-TAU	Optical depth, mean effective radius
ECMWF	Temperature, pressure, specific humidity, surface winds

Table 1: Data products and variables used in research from 2007-2010

To identify low clouds, the 2B-GEOPROF-LIDAR product (Mace et al. 2009) is used. This product combines the significant echo mask from the radar-only 2B-GEOPROF retrieval product (Marchand et al. 2008) and the LIDAR vertical feature mask (Vaughan et al. 2009) to create a merged cloud mask that detects up to five cloud layers per CPR vertical profile (Mace et al. 2009). The cloud mask indicates whether each pixel detected by the CPR is either clear or cloudy by assigning a cloud probability to each of the pixels, with threshold values greater than 20 indicating a cloud (Mace et al. 2009).

To describe the characteristics of the clouds across the transition, the CloudSat 2B-TAU products are used to determine the mean cloud optical depth and effective

radius. The optical depth of the cloud is a measure of how much radiation is able to pass through a cloud layer without getting reflected or absorbed, or how transparent a cloud is to radiation (Bodhaine et al. 1999). The geometric thickness of a cloud is related to the optical depth, where a thicker cloud will have a higher optical depth. The particle size and concentration is also a factor in determining the optical depth, as clouds with higher concentrations of large particles will result in a higher optical depth (Szczodrak et al. 2001). Also, the likelihood of precipitation may also affect the optical depth of a cloud, where heavily precipitating clouds will have a higher optical depth than non-precipitating clouds. The 2B-TAU algorithm uses a Bayesian estimation approach (Marks and Rodgers 1993) with forward calculations to calculate the optical depth and effective radius estimates from CloudSat radar measurements, with the addition of measurements from MODIS and reanalysis data from ECMWF during the day (Polonsky 2008; Hamanda and Nishi 2010; Nakajima et al. 2010).

The CloudSat Radar-Visible Optical Depth Cloud Water Content Product (2B-CWC-RVOD) uses a forward model to retrieve estimates of the vertical profile of cloud water content for each radar profile measured by CPR (Austin et al. 2001; Marra et al. 2013). The cloud liquid water path (LWP) is calculated from 2B-CWC-RVOD as the integrated liquid water content (LWC) estimated throughout a cloud column (Wood and Taylor 2001). This product produces more accurate results than the radar only (2B-CWC-RO) product as it uses a combination of the radar reflectivity factor from the 2B-GEOPROF product and visible optical depth estimates from the 2B-TAU product to constrain cloud retrievals more tightly (Deng 2005; Devasthale and Thomas 2012;

Rajeevan et al. 2012). One caveat is that 2B-CWC-RVOD has been shown to have significant errors in the presence of precipitation (Christensen et al. 2013). For this reason, only non-precipitating cloud LWP is analyzed in this study.

Two products from CloudSat will be used to estimate precipitation in stratocumulus clouds in the study domain. Because the CPR is sensitive to small water droplets, even developing precipitation can be detected, which cannot be said for other spaceborne precipitation radars like the TRMM PR (Stephens and Haynes 2007). The 2C-PRECIP-COLUMN and 2C-RAIN-PROFILE are used to detect precipitation and quantify surface precipitation, respectively. The 2C-PRECIP-COLUMN product contains a precipitation flag that uses radar reflectivity thresholds to distinguish non-precipitating scenes from scenes where precipitation is possible and defines four categories: non-precipitating, rain possible, rain likely, and rain certain (Haynes et al. 2009; Lebsock et al. 2011). However, since ground clutter contaminates the bins below 720m, the 2C-PRECIP-COLUMN product has difficulty detecting rain in low-level clouds below 720 m (Rapp et al. 2013).

Whereas the 2C-PRECIP-COLUMN product identifies the likelihood of precipitation, the 2C-RAIN-PROFILE product focuses on quantitative precipitation estimation in low clouds. This product uses the CPR reflectivity profile and the path integrated attenuation (PIA), which accounts for the energy loss between the CPR and the range gate from extinction processes, to retrieve the vertical distribution of rainwater (Mitrescu et al. 2010; Lebsock and L'Ecuyer 2011) and contains several improvements over the early quantitative estimates of precipitation by CloudSat. This retrieval product

includes a visible optical depth constraint from MODIS, a model for the evaporation of rain that occurs directly beneath the cloud layer (similar to a model from Comstock et al. 2004), and raindrop size distributions that are more representative of warm rain processes (Lebsock and L'Ecuyer 2011). These improvements are especially important for boundary layer clouds in this region and validation against in situ radar estimates shows generally good agreement (Rapp et al. 2013).

Because the radiative feedbacks are so important to the development and maintenance of stratocumulus and shallow cumulus clouds and top of atmosphere shortwave cloud forcing is so important for capturing climate sensitivity, this study uses the new 2B-FLXHR-LIDAR product which incorporates measurements from the CPR, CALIPSO, and MODIS to estimate the broadband fluxes and heating rates for each CloudSat radar profile along the trajectory. The 2B-FLXHR-LIDAR product builds off the 2B-FLXHR approach, but the revised product also makes use of the CALIPSO vertical feature mask through CloudSat's 2B-GEOPROF-LIDAR product (Mace 2007; Marchand et al. 2008) to detect low clouds missed by CloudSat. The cloud radiative effect on the shortwave fluxes at the top of the atmosphere (TOA_CRE) in the shortwave is calculated by determining the difference between clear and cloudy conditions (Charlock and Ramanathan 1985; Hartmann et al. 1986). The rate of radiative heating is determined by calculating the amount of flux that is either absorbed or emitted within each cloud layer in the vertical profile.

The ECMWF-AUX uses environmental profiles of pressure, temperature, and specific humidity from European Center for Medium-Range Weather Forecasting

(ECMWF) analyses, which are then interpolated to each CloudSat vertical bin (Lebsock and L'Ecuyer 2011). The importance of these variables is highlighted in Figure 1 as each variable influences the formation and development of marine stratocumulus clouds and could play a leading role in the transition to cumulus clouds. There are some shortcomings with using reanalysis data, however, where the data from ECMWF is comprised of analysis data that is only updated every 6-12 hours and is prone to biases due to inadequate vertical resolution (Yue et al. 2013).

2.2 Methods

The area of interest for this study is the southeast Pacific Ocean (SEP). Specifically, this study examines low-level clouds on a 2° x 2° grid from 30°S-5°N and from 85°W-110°W, excluding any cloudy scenes over land. These boundaries were chosen because they not only encompass the climatological trajectories from Sandu et al. (2010), but also because of the number of recent field campaigns studying the marine stratocumulus clouds that dominate this region. Unlike scanning instruments like MODIS, CloudSat's non-scanning nadir-viewing CPR limits with the number of times the study region is sampled both day and night, so longer temporal averaging is necessary to collect enough observations for an accurate representation of the region for this analysis. Rapp et al. (2014) found that the spacing of the grid boxes allows for the optimal representation of the climatological representation because any smaller sized grid boxes would result in more noise in the data collected and if the grid boxes were larger, the structure of the clouds and localized effects along the trajectory would be

missed. Therefore, this study analyzes satellite data from 1 January 2007 to 31 December 2010 to aggregate enough observations to develop a more complete representation of cloud properties, precipitation, and radiative effects of this cloud system. This analysis will provide a detailed description of the climatological cloud, precipitation, and radiative characteristics across the transition in low-level stratocumulus clouds as they break up into cumulus clouds in the southeast Pacific.

2.2.1 Low cloud identification

First, the four years of CloudSat, CALIPSO, and environmental data are extracted from the files listed in Table 1 and processed within the southeast Pacific region defined above. For this analysis, a profile is considered cloudy if there is at least one cloud layer detected in 2B-GEOPROF-LIDAR. Since this study is only interested in stratocumulus and shallow cumulus low-level clouds, the analysis is limited profiles with cloud heights below 4 km. This boundary is chosen because stratocumulus clouds rarely exceed 2 km; however, convective shallow cumulus can penetrate through this low cloud layer (Comstock et al. 2005) and disorganized shallow cumulus cloud heights increase as the boundary layer deepens near the equator (Bretherton et al. 2003). For this analysis, cloudy scenes where only a single layer of clouds is detected from the CPR are the primary data source. One problem that may arise from the use of single layer clouds is the contamination of overlying cirrus clouds, with its impact felt most near the equator where deep convection is more prominent. The overlying cirrus associated with anvils

from deep, convective clouds along the Intertropical Convergence Zone (ITCZ) will impact our ability to capture the full effect of the shallow cumulus clouds.

2.2.2 Cloud, radiative, and environmental properties

To understand the macrophysical and microphysical cloud characteristics of stratocumulus as they transition into shallow cumulus clouds, the CloudSat 2B-GEOPROF-LIDAR, 2B-TAU, and 2B-CWC-RVOD products are used. The 2B-GEOPROF-LIDAR retrieves up to five cloud layers in each vertical profile (Mace et al. 2009). If at least one cloud layer is detected and the cloud top height of the highest layer falls below the 4 km boundary set for this study, the cloud layer base and top height are recorded and the profile containing low clouds is analyzed. The profiles that meet these criteria are then used to calculate the low cloud fraction, which is important for analyzing how the macrophysical structure of the stratocumulus cloud system changes as they break apart into shallow cumulus clouds. The cloud fraction for a given level in the vertical profile is defined as the number of cloud observations detected within a cloud layer divided by the total number of observations in that cloud layer. To calculate the total grid box cloud fraction, the total number of cloud observations within a grid box is divided by the total number of observations in that grid box.

Because the presence of precipitation leads to overestimations in some variables (Wood 2008), only cloud variables from 2B-CWC-RVOD and 2B-TAU that contain no precipitation are analyzed. The mean liquid water path is calculated as the sum of all valid liquid water path retrievals divided by the number of cloud observations in that grid box. The mean optical depth and effective radius follow the same process as the

calculation for the LWP, where the total of the values for each variable in that grid box is divided by the number of cloud observations in that grid box. Because the retrieval of effective radius and optical depth require MODIS visible reflectances, they are only calculated during the day, whereas the mean LWP is calculated both day and night since it can be retrieved solely from the CPR reflectivity profiles.

To study precipitation across the transition, the CloudSat 2C-RAIN-PROFILE near-surface precipitation estimate and the 2C-PRECIP-COLUMN precipitation occurrence flag are used. For this analysis, the confidence flag from 2C-PRECIP-COLUMN is used to calculate the frequency of precipitation. The confidence flag ranges from no precipitation detected (when the precipitation flag (pflag) = 0) to certain rainfall detected (pflag = 3). To test the sensitivity of the confidence flag, we compare the frequency of whenever rainfall is possible (pflag = 1) to when rainfall is certain (pflag = 3). The frequency of precipitation in both cloudy scenes and in all (cloudy sky + clear sky) scenes is calculated as the total number of times precipitation with a given confidence flag (either 1 or 3 in this case) divided by either the total number of observations in that grid box or the total number of cloud observations detected in that grid box. The rain rate retrieval from the 2C-RAIN-PROFILE quantifies the intensity of drizzle. Clouds are considered to be precipitating when the 2C-PRECIP-COLUMN identifies a profile as ‘rain certain’ and the 2C-RAIN-PROFILE has a rainfall rate greater than zero. This analysis considers both the conditional and unconditional rain rate. The unconditional rain rate is the sum of all values of rainfall intensity divided by the total number of observations from each grid box. The conditional rain rate is

calculated from the sum of the estimated rainfall intensity and divided by the total number of precipitating observations in that grid box.

Cloud top longwave cooling is important for the development and maintenance of stratocumulus and has been found to strongly influence the turbulence that occurs within the stratocumulus cloud layer (Bretherton et al. 2010). Shortwave heating rates during the day are also important since they describe the absorption that occurs at the top of the cloud layer, which helps to break up the clouds. The cloud radiative effect in the shortwave is important for understanding the radiative impact clouds have on the top of the atmosphere and how they influence Earth's radiation budget (Charlock and Ramanathan 1985). The 2B-FLXHR-LIDAR product is used to examine the longwave and shortwave heating rates, as well as upwelling and downwelling fluxes, paying special attention to the cloud top longwave cooling across the transition and the shortwave radiative impact of clouds. The amount of cooling at the cloud top is calculated by dividing the sum of all longwave cooling rates from each cloud top observation by the total number of cloud observations. The same process is repeated for the shortwave heating at the cloud top; however, only daytime scenes are considered. The shortwave TOA_CRE is calculated from the difference in radiative fluxes between cloudy conditions and clear-sky conditions (Hartmann et al. 1986).

The environmental profiles are important to examine as the clouds advect equatorward where waters are warmer and shallow convection is more favorable. The temperature and humidity profiles describe the structure of the boundary and inversion layers as they evolve throughout the transition process. Surface wind, relative humidity,

and surface temperature help to improve the understanding of the environment at the surface by determining the surface latent heat flux, which is the key source of moisture to the lower level clouds (Hartmann 1994; Wood 2012). To describe the thermodynamic conditions across the transition, the ECMWF-AUX product is used, which provides atmospheric temperature, pressure, and humidity profiles, as well as the surface wind speed and the sea surface temperatures from the ECMWF analyses that have been collocated with CloudSat. It should be noted here that the data from ECMWF is comprised of analysis data that is only updated every 6-12 hours and is prone to biases (Yue et al. 2013); however, this dataset provides the most complete representation of the clouds' environment given the lack of actual observations available for this analysis. To calculate the mean atmospheric profiles in the study, the environmental data is summed over each level in the vertical profile between the surface and 4 km and then divided by the total number of observations for each vertical profile layer.

Lower tropospheric stability (LTS) is a measure of strength of the inversion layer found above the boundary layer where stratocumulus clouds develop (Wood and Hartmann 2006). LTS, shown in Equation (1), is the difference between the potential temperature the 700mb level, or free troposphere, and the surface (Slingo 1987; Klein and Hartmann 1993). Similar to the other variables, the mean LTS is calculated as the sum of all cloud observations within each grid box divided by the total number of cloud observations in that box.

$$LTS = \theta_{700} - \theta_{sfc} \quad (1)$$

2.2.3 Climatological trajectory analysis

Using the 4-year dataset developed for the larger southeastern Pacific domain, we follow an approach similar to Sandu et al. (2010) and analyze data along the climatological trajectory locations described in the appendix of their paper. Sandu et al. (2010) showed that the spatial structure of the climatological trajectories capture the evolution of the airmasses and are therefore, useful for studies on the transition from stratocumulus to shallow cumulus clouds. Figure 5 from Sandu et al. (2010) illustrates the medians of selected forward and backward trajectories calculated in the southeast Pacific Ocean. Figure 6 shows the points that were calculated along the trajectory after a linear fit between the coordinates from Sandu et al. (2010). Because of CloudSat's near-nadir only sampling, 2°x 2° boxes are defined around each of our trajectory data points in Figure 6 to aggregate enough data for the climatological representation of the clouds throughout the transition. The asterisks are trajectory points used for this study and the plus signs are the data trajectory points from Sandu et al. (2010). The lines found on each side of the data points in Figure 6 represent the endpoints for the 2°x 2° boxes used in this study. Data in each of these grid boxes is analyzed throughout the 4-year period to characterize the climatology and interannual variability in cloud properties, precipitation, and radiation effects along the climatological transition trajectory. Table 2 lists the coordinates along the trajectory and the total number of observations for the four-year period in each coordinate grid box.

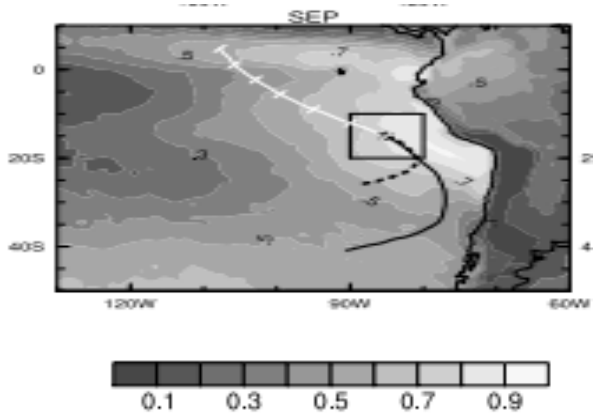

Figure 5: Cloud fraction on the third day of the selected trajectories, and medians of the forward (white line) and the backward (black line) climatological trajectories in the southeast Pacific and Atlantic Oceans. (Sandu et al. 2010)

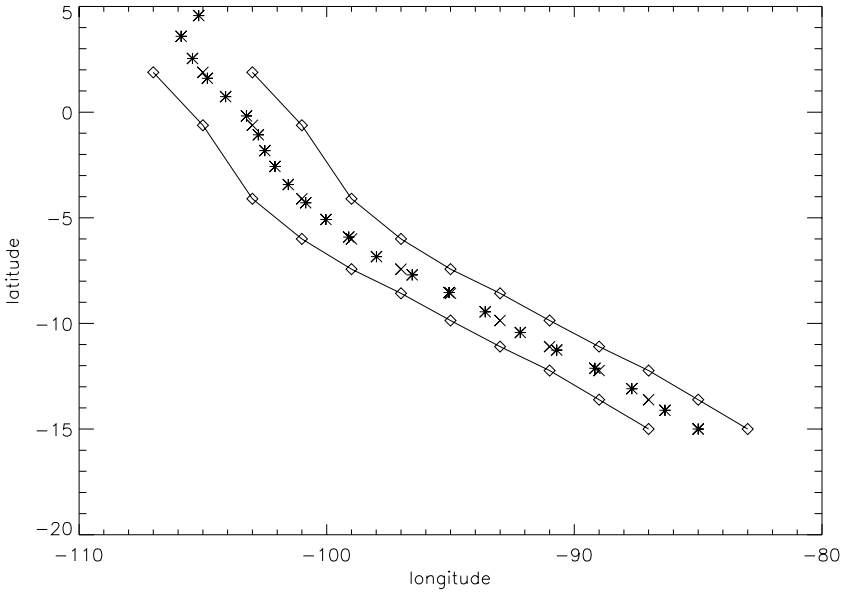

Figure 6: Trajectory coordinate points (*) with the 2°x 2° boxes around each of the trajectory data points (*).The other points (+) are trajectory points calculated from the Appendix of Sandu et al. (2010).

Latitude	Longitude	Total # of Observations
-85.000	-15.000	36533
-87.000	-13.608	28803
-89.000	-12.231	35743
-91.000	-11.096	35020
-93.000	-9.864	43615
-95.000	-8.577	41926
-97.000	-7.431	33146
-99.000	-6.001	32722
-101.000	-4.106	28847
-103.000	-0.625	32335
-105.000	1.882	42628

Table 2: List of coordinate points used in study and the total number of observations collected within each 2°x 2° box around each coordinate.

The annual mean climatology of each variable is computed for each of the 4 years to observe the mean key features of stratocumulus clouds and shallow cumulus clouds. The interannual variability is then analyzed by comparing the 4 years to each other to distinguish any major differences between the years. It is important to examine the year-to-year fluctuations for the different cloud, environmental, and radiative variables for any distinctive features in particular years that differ from the four-year mean pattern. Because there is a large seasonal cycle in cloud amount (Klein and Hartmann 1993), data is analyzed seasonally by grouping the data in three-month

periods for all years to describe the intraseasonal variability in transition features. To represent each season for all years, the months are grouped together as March/April/ May (MAM), June/July/August (JJA), September/October/November (SON) and December/January/ February (DJF).

Cloud fraction and precipitation have also been shown to peak during the nighttime and early morning hours (Klein et al. 1995; Rapp et al. 2013), so analysis of the diurnal variability in cloud properties across the stratocumulus to cumulus transition is also performed. For this analysis, the data is divided at 1200 UTC, near sunrise. Thus, anything before 1200 UTC is considered night and anything after 1200 UTC is considered day. It should be noted that this analysis does not represent the full diurnal cycle, but rather represents the day/night differences between observations at the CloudSat overpass times, which occur in the very early morning and early afternoon.

3. RESULTS

3.1 Climatological representation

The four-year means calculated along the climatological trajectory for each of the variables are first investigated. The first variables discussed are the atmospheric profiles, followed by the cloud properties, precipitation, and finally, the radiative variables.

The four-year mean climatology of the environmental profiles up to 3 km is shown in Figure 7a-d. The SSTs in Figure 7a show an overall increase in temperatures as the trajectory moves equatorward. Just south of the equator, temperatures decrease because of the equatorial cold tongue, a feature where enhanced mixing from the equatorial currents and horizontal large-scale wind patterns cause a significant drop in the SSTs (Wallace et al. 1989; Moum et al. 2013). The corresponding atmospheric temperature profile is shown in Figure 7b with near-surface values ranging from 290 K at 15°S to 296 K near the equator. A temperature inversion is present between 1.1 - 1.5 km and is strongest in the southern region where the mean inversion in the ECMWF analysis is about 4 K. The inversion strength in this study is likely underestimated based on in situ results from previous studies that have shown the low vertical resolution in models and reanalysis (Rahn and Garreaud 2011) leads to underestimates of the inversion strength. The lower tropospheric stability (LTS) is shown in Figure 7c with the greatest stability at the southernmost point of the trajectory and decreasing stability approaching the equator, due to the deepening boundary layer and increased SSTs. The specific humidity in Figure 7d features the greatest humidity near the surface in the

northern portion of the study region and lowest values of moisture above the boundary layer in the southernmost portion of the study region. A stronger vertical gradient is noticeable at the top of the boundary layer farther south where cool and dry, subsiding air is present and the temperature inversion is much stronger (Norris and Klein 2000).

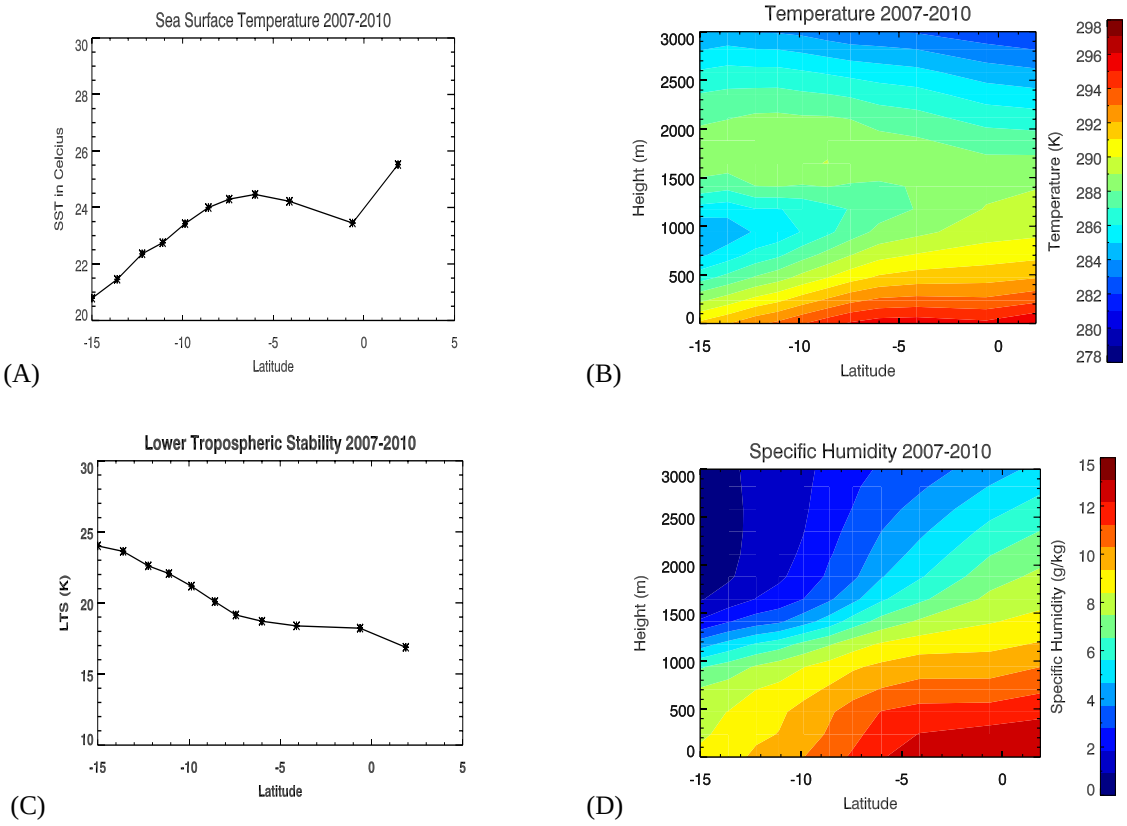

Figure 7: Four-year mean representation of the environmental variables (a) SST in °C (b) temperature profile (K), (c) the LTS (K), and (d) specific humidity (g kg^{-1}), along the climatological wind trajectory in the southeast Pacific.

The four-year means for each of the cloud variables are shown in Figure 8a-e. The vertical profile of cloud fraction below 3 km in Figure 8a shows that the greatest percentage of clouds is located around 1 km, with higher values are seen in the southernmost grid boxes where persistent stratocumulus cloud decks are commonly located. The fraction of clouds decreases throughout the vertical profile just south of the equator indicating the transition to a shallow cumulus regime. To facilitate comparison with past studies using other non-profiling instruments, the total low cloud fraction, defined as the total number of cloud observations divided by the total number of observations in a grid box, is shown in Figure 8f. Again, it shows a gradual decline in low clouds over the transition, with a minimum located just south of the equator. The single layer cloud top and base heights in Figure 8b show relatively constant mean heights along the trajectory, with only a small dip in the cloud top height. Cloud top heights for the single layer are normally around 1.5 km with the lowest value around 1.4 km whereas the cloud base heights remain constant around 0.65 km. The reduction in cloud fraction just south of the equator is likely due to the equatorial cold tongue positioned off the Peruvian coastline where lower SSTs are found in contrast to the higher SSTs throughout the tropical regions (Mansbach and Norris 2007). The strong temperature inversion and increased LTS values in the southernmost portion of the study region correspond well with the greater cloud fractions. As the trajectory approaches the equator, SSTs are warmer and the subsidence is reduced, causing a weakening in the inversion as the stratocumulus cloud decks break apart and allow convective shallow cumulus with lower cloud fraction to dominate the region. Near the equator the breakup

of the stratocumulus deck from the weaker subsidence and inversion layer is evident as the cloud fractions drop considerably, but the fraction of deeper, more convective clouds increases. The average change in the low cloud fraction from the peak and minimum amount of clouds is also calculated to consider the speed of the transition period and how it varies along the trajectory from year to year. A steady reduction in the total low cloud fraction is observed throughout most of the trajectory, however the minimum in cloud fraction varies between 10° S and 5°S interannually as this region is where the low cumulus clouds develop under the thinning stratocumulus deck. The speed of the transition changes rapidly around 5°S as cumulus clouds develop more near the ITCZ, as shown in the low cloud fraction climatology. A number of factors play a role in where the minimum amount of clouds occurs along the trajectory, as the time it takes the transition from stratocumulus to cumulus may vary from year to year.

The next three figures are closely related to one another, as the optical depth of a low cloud is proportional to the LWP and inversely related to the effective radius (Stephens et al. 1978). Figure 8c shows the LWP for non-precipitating clouds, where the four-year mean LWP values are between 100-175 mg m^{-3}. There are lower LWPs in the southern coordinate points that increase closer to the equator, with the higher LWP values around 5°S closely corresponding to the increased amount of deeper clouds seen in Figure 8a-b. The optical depth in Figure 8d varies along the trajectory with the highest values of about 17 found at 15°S and 4°S and the lowest value of about 9 just south of the equator. The trends found in the optical depth are also evident in the cloud fraction in Figure 8a where values of optical depth on average are lower close to the equator and

highest near the southern boundary of the study region. The effective radius in Figure 8e ranges from 14-18 μm throughout the trajectory.

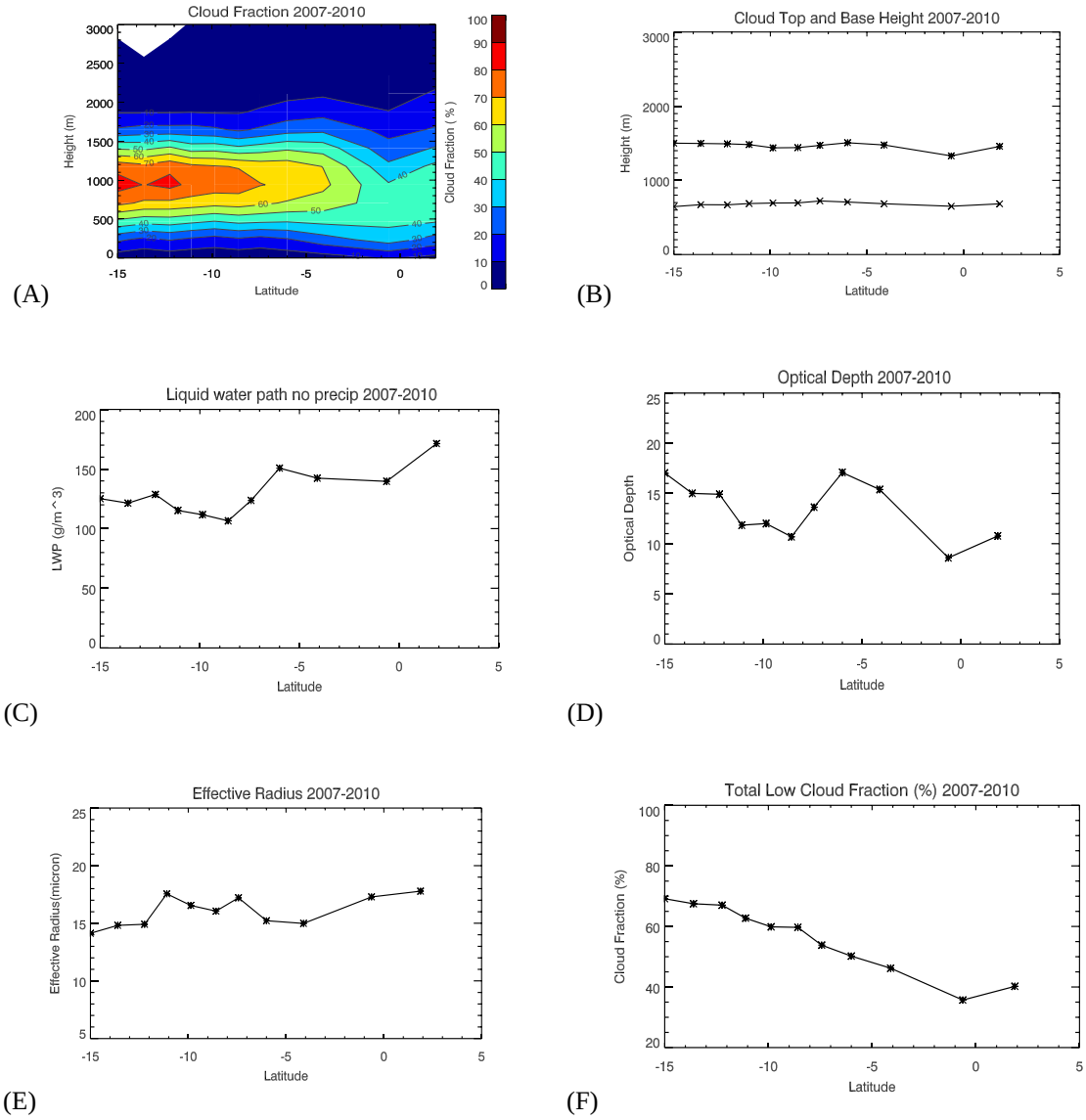

Figure 8: Four-year mean representation of each cloud variable observed along the climatological wind trajectory in the southeast Pacific. The panels are (a) cloud fraction (%), (b) cloud layer top and base heights (m), (c) optical depth during the day (unitless), (d) effective radius during the day (microns), (e) non-precipitating cloud liquid water path (g m^{-2}), and (f) total low cloud fraction (in %).

The greatest variability in the effective radius, cloud fraction, and other environmental variables is found between 12°S and 6°S, likely due to the transition that takes place as the large scale subsidence decreases, the inversion layer begins to weaken, and the shallow cumulus clouds begin to develop beneath the dissipating stratocumulus cloud deck as the boundary layer weakens and deepens. The overall trend is a slight increase in effective radius and liquid water path toward the equator. The optical depth features more noise compared to the previous two variables, but increased close to the equator where the cloud layer is thicker and LWP values are greater. Both the effective radius and the optical depth are retrieved similarly using radar reflectivity (Polonsky et al. 2008), therefore changes in these variables should in turn affect the LWP. There appear to be inconsistencies between the mean cloud optical depth, LWP, and effective radius near the equator; however, the effective radius and optical depth are not retrieved at night, unlike LWP. At night LWP is retrieved without the optical depth constraint, therefore, the results for the optical depth and effective radius do not follow the expected relationship with LWP.

Another potential limitation of using CloudSat-retrieved properties is that the CPR is unable to detect clouds in the lowest 2-3 bins because of ground clutter; therefore, when cloud bases extend below about 720 m, retrieved integrated quantities like LWP and optical depth may be underestimated. The cloud fraction in Figure 8a shows where some of the greatest impacts are likely, as clouds, though fewer, are often found below 720 m near to the equator. To verify the CloudSat retrievals, a brief

comparison of the LWP, effective radius, optical depth, and cloud fraction climatological results to the level 3 MODIS (MOD08_M3.051) products was performed (not shown). Overall, the MODIS retrievals for optical depth, effective radius, and LWP show general agreement between the cloud variables, as MODIS values for the effective radius are lower on average than the CloudSat retrievals but only by about 10 %, although MODIS values are significantly lower for the LWP and optical depth, with a difference greater than 30 %. A lack of agreement between MODIS and CloudSat retrievals is found around 6°S where a significant increase in LWP and optical depth is not detected by MODIS, but it is likely not an artifact because in this area, the SST is relatively high and there is more frequently occurring shallow convection, resulting in an increase in LWP and optical depth. The MODIS products used for comparison also did not have the 4 km cloud top height, single layer, and non-precipitating restrictions, which could also account for some of these differences.

The four-year mean climatology for the rain frequency and rain rate for all observations are shown in Figure 9a and 9b, respectively. The rain possible frequency for cloudy scenes (blue line) is the likelihood that radar reflectivity is between -15 and -7.5 dBz, whereas the rain certain frequency for cloudy scenes is the likelihood that radar reflectivity is greater than 0 dBz. Precipitation in clouds with tops less than 4km is more frequent in the southern portion of the study area, with rain possible in nearly 30% of observations at 15°S. Values decrease as the trajectory approaches the equator and reach a minimum just south of the equator due to the lower occurrence of clouds observed in Figure 8a as the stratocumulus cloud deck advects equatorward over the SST cold

tongue. Precipitation frequency begins to increase once the trajectory moves north of the equator as temperature and humidity increases and deeper shallow convection is more common. Figure 9b shows the conditional rain rate along the four-year mean trajectory. The conditional rain rate is calculated as the average rain rate from all rain certain observations with the highest rain rates near the equator that are associated with several other variables shown in the previous figures, such as the lower cloud fraction, higher LWP values, and more frequent deeper clouds. These factors indicate that the dominant cloud regime over this region is no longer stratocumulus, but convective shallow cumulus.

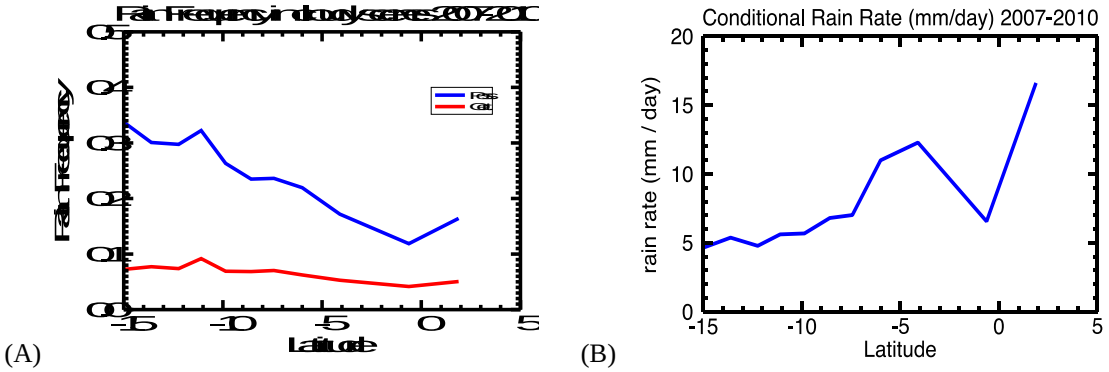

(A) (B)

Figure 9: Four-year mean for (a) the rain frequency (% likelihood) and (b) the rain rate (mm d^{-1}).for all cloud observations .The red and blue lines in figure 9(a) represent the likelihood that rain is present at the surface over all observations (blue) and the likelihood that rain is certain at the surface over all observations (red). The rain rate in Figure 9(b) is separated by the conditional (blue) rain rate and the unconditional (red) rain rate (mm d^{-1}).

When the temperature inversion is strongest, the LTS, cloud fraction, and cloud layer thickness are greatest and the SST is at a minimum. The air is also driest over this area as dry air from the downward branches of the Hadley cell subsides over the strong inversion layer. Environmental conditions over the southern region display warm and dry, subsiding air over cooler SSTs, allowing for a strong temperature inversion to be in place under stable conditions. The strong inversion and stable conditions over the cooler waters allow for the formation of thick, low lying clouds, resulting in large cloud fractions over the southern region. The environmental conditions in this region are also the more favorable for the development of drizzle. As the winds advect equatorward the stability decreases and the moisture values increase throughout the profile, weakening the inversion. It is interesting to note around 6°S where there is a slight increase in the SST, LWP, and optical depth, and a decrease in the LTS. The change in cloud fraction over this area is also greatest as there are more frequent deeper clouds which infer the likely development of shallow cumulus clouds into stratocumulus clouds overhead, however the data products used in this analysis inhibits this study from seeing the individual components of these clouds. This process is seen in the bottom panel of Figure 2 where the shallow cumulus develop beneath and eventually penetrate the overlying stratocumulus deck. Under these warmer and less stable conditions, the percentage of clouds decrease but the LWP, optical depth, and precipitation rates increase as the shallow cumulus clouds develop and eventually evolve into the dominant cloud regime.

The four-year means for some of the cloud radiative variables, the cloud radiative effect at the top of the atmosphere (TOA_CRE), longwave cloud top cooling, and shortwave radiative heating, are shown in Figure 10a-c. Because the shortwave cloud effect is so important for climate and estimating climate sensitivity, we focus on the grid box mean shortwave TOA_CRE for all scenes is shown in Figure 10a to determine the cloud impact on the shortwave fluxes at the top of the atmosphere. Values range from -150 to -50 W m^{-2} with stronger values away from the equator where cloud fractions are high and more shortwave radiation is reflected. The weakest shortwave TOA_CRE is near the equator even though the LWP is greater over the region, showing the dominance of the effects of reduced cloud fraction.

The cloud top radiative cooling and heating rates directly impact the convection of the cloud layer and the amount of turbulence that occurs within the cloud (Lilly 1968; Wood 2012). The longwave cooling at the cloud top drives the instability of the cloud layer (Lilly 1968; Wood 2012) and is shown in Figure 10b, where there is an overall steady increase in values from -30 K d^{-1} at 15°S to values closer to -10 K d^{-1} near the equator. Shortwave heating at the cloud top, shown in Figure 10c, directly influences the diurnal variability of these clouds as they absorb incoming solar radiation (Turton and Nicholls 1987; Wood 2012). The range is much smaller than the longwave cooling, with values decreasing from about 7 K d^{-1} in the southern trajectory points to about 4 K near the equator with a small increase as the trajectory crosses the equator. It is interesting to note the similarity in the trends between both the longwave cooling and shortwave heating at the cloud top and the total low cloud fraction in Figure 8f, where a decrease

cloud top heating in the shortwave or cooling in the longwave corresponds to a decrease in fraction of low-level clouds. Therefore, as the longwave cooling decreases, the turbulence needed to maintain the cloud also decreases, resulting in a reduction in cloud cover.

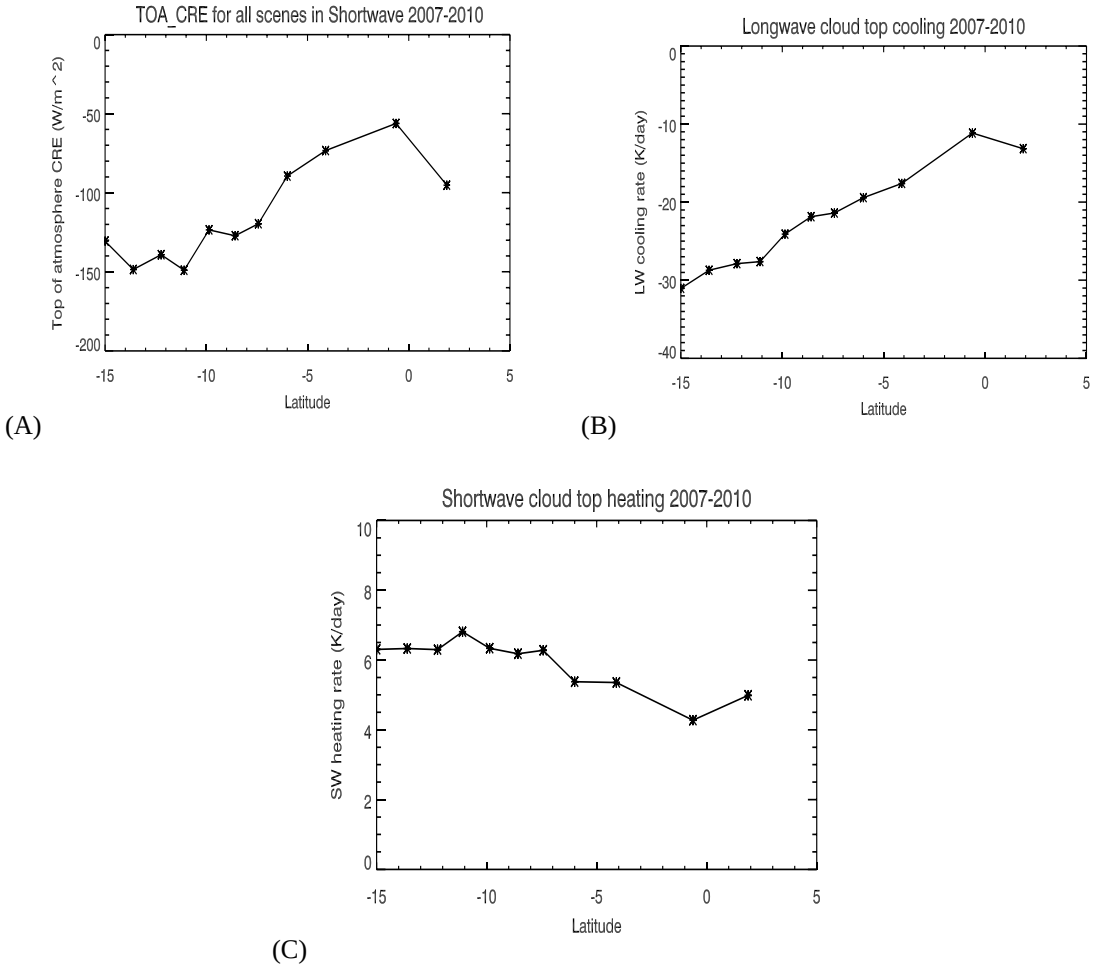

Figure 10: Four-year mean along the climatological wind trajectory in the southeast Pacific for (a) longwave cloud top cooling (K d^{-1}), (b) shortwave cloud top heating (K d^{-1}), and (c) top of atmosphere shortwave cloud radiative effect (Wm^{-2}).

3.2 Interannual variability

To better understand the year-to-year fluctuations in the environment, clouds, and radiation compared to the four-year mean climatology, the interannual variability from 2007-2010 is examined. Because some of the results are very similar to the four-year climatology, only certain variables that highlight interesting interannual differences will be discussed in the remaining sections.

The environmental profiles in Figures 11-14 show some year-to-year variability in properties important for these clouds and their transition. The SST in Figure 11 shows little interannual variability throughout the four years in the southernmost latitudes, but 2007 differs in that the SSTs were considerably lower near the equator compared to the other three years. In 2007 the SSTs in this region do not exceed 25°C and the decrease in temperature between 6°S and 1°S is sharper than all other years. This suggests that the equatorial cold tongue was considerably stronger this year, likely due to the La Niña event in the latter half of 2007 (Su and Jiang 2013). The interannual variability of the temperature profile in Figure 12 a-d shows that the temperature inversion was strongest in 2010 and 2007 compared to the other two years. In both years, temperatures in the boundary layer are cooler, and the subsiding air above the cloud layer is drier and warmer than in 2008 and 2009, resulting in a stronger inversion over the southern domain. The El Niño-Southern Oscillation (ENSO) phenomena may have a significant impact on the environmental conditions over this study region as it impacts the strength and placement of the Walker Circulation and the subtropical high (Julian and Chervin 1978; Rassmuson and Wallace 1983). These conditions could be the result of the shift

from El Niño events to La Niña events that took place during austral spring in both years, which impacts the large scale circulation in a variety of ways depending on the location, strength, and sign of the ENSO event. For 2007, a weaker El Niño occurred in the central Pacific, with a La Niña developing in the late August. For 2010, the stronger temperature inversion in the southern latitudes is likely related to the quick transition from El Niño to La Niña in July 2010, which reached its peak in early 2011 (Su and Jiang 2013).

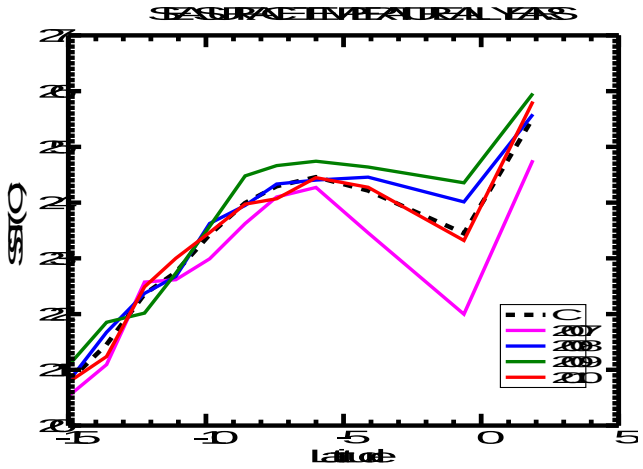

Figure 11: The sea surface temperature (°C) along the climatological wind trajectory in the southeast Pacific for each year relative to the 4-year mean (black dashed).

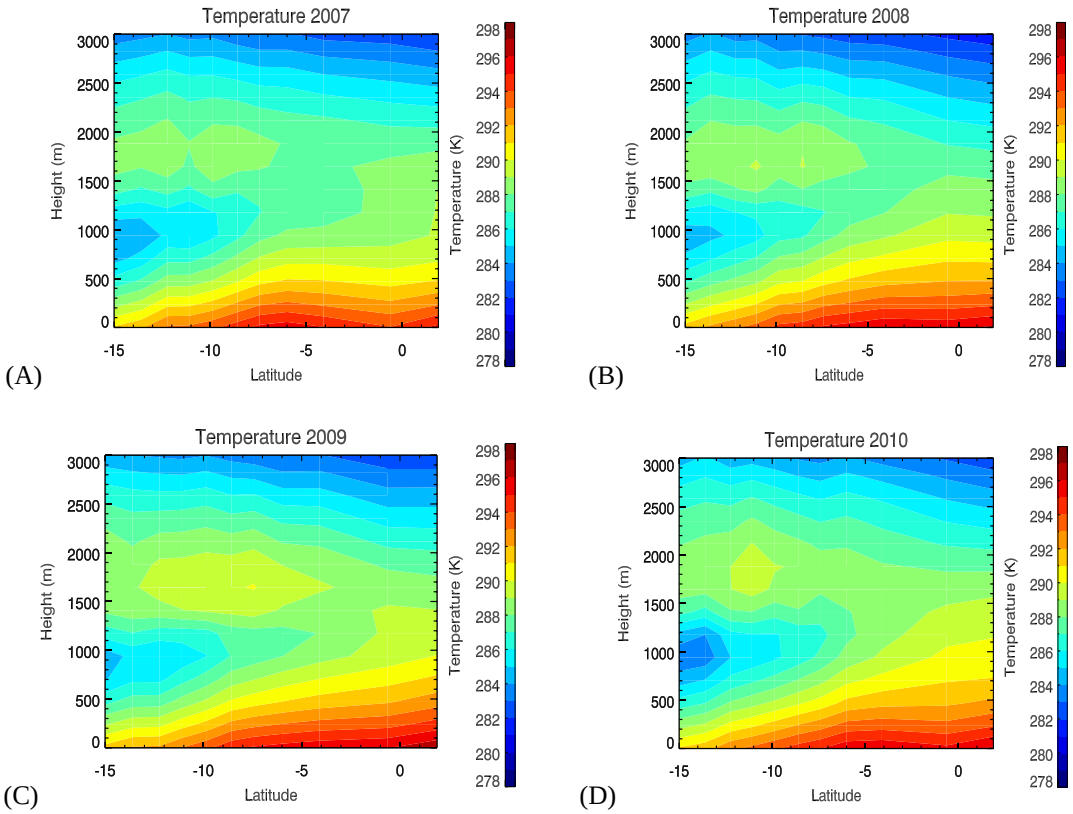

Figure 12: The temperature profile (K) along the climatological wind trajectory in the southeast Pacific for 2007-2010.

The LTS for all years is compared to the four-year mean in Figure 13 where 2010 and 2007 show the greatest stability along the trajectory. The LTS for 2010 is greatest in the southern part of the domain where the temperature inversion is strongest with strong subsidence aloft and cooler SSTs. The LTS for 2007 is greatest near the equator where the equatorial cold tongue is strongest for all years.

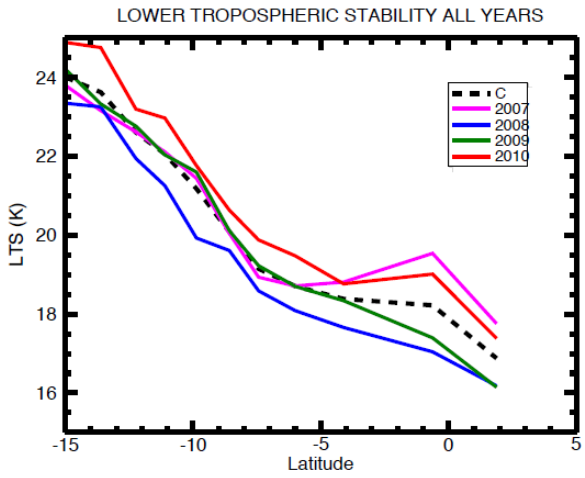

Figure 13: The LTS (K) for each year relative to the 4-year mean climatology (black dashed).

The specific humidity interannual variability in Figure 14 a-d suggests stronger subsidence in 2007 and 2010 compared to 2008 and 2009, as much dryer conditions are found above the inversion layer. In 2010, the specific humidity values are low around 15°S but the moisture does expand upward closer to the tropics where convection is more favorable. In 2007, dry air is persistent along the trajectory, as the enhanced subsidence keeps the moist layer shallow throughout the transition.

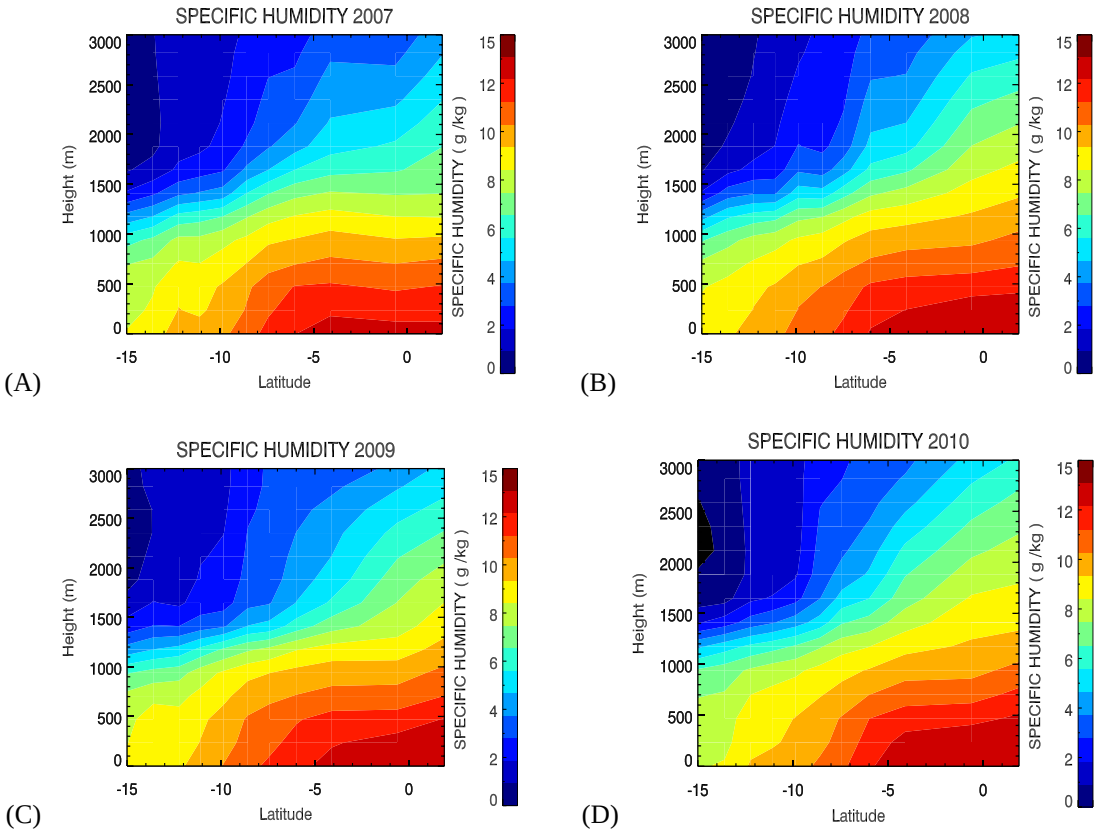

Figure 14: The specific humidity (g kg^{-1}) along the climatological wind trajectory in the southeast Pacific for 2007-2010.

Corresponding cloud variables that illustrated interesting features in the interannual variability include the cloud fraction, cloud top and base heights, and the LWP. The cloud fraction transition for each year in Figure 15 a-d is well correlated to the LTS in Figure 13 as the amount of stability contributes to the development of the cloud deck and the fraction of clouds. The LTS for 2010 is stronger than the other years in the southern portion of the domain, resulting in the higher cloud fraction observed over the same region in 2010. Also, the minimum LTS corresponds to the region where the cloud fraction is lowest. The year-to-year differences for both variables are greatest between

5°S and the equator, where each year displays a different feature. Again, the two years that display the greatest deviation from the four-year mean cloud fraction are 2007 and 2010, during the years that El Niño transitioned to La Niña during the austral spring. In 2007, the overall cloud fraction over the southern regions are lower than the other years, which is consistent with the weaker LTS values. The cloud fraction approaching the equator in 2007 is greater and is consistent with the enhanced stability and the lower SSTs in Figure 11, likely due to a stronger equatorial cold tongue. For 2010, strong subsidence and increased stability is detected over the southern portion of the region where a strong temperature inversion is in place. However, these values change rapidly along the trajectory as cloud cover rapidly declines during the transition and deeper clouds develop more frequently. These results suggest that an earlier transition takes place with the breakup of stratocumulus clouds and development of shallow cumulus occurring further south in 2010 than in previous years. The total low cloud fraction change over 100 km is also calculated to consider the speed of the transition period and how it varies along the trajectory from year to year. A steady reduction in the total low cloud fraction is observed throughout much of the trajectory, however the minimum in cloud fraction varies between 10° S and 5°S interannually as this region is where the low cumulus clouds develop under the thinning stratocumulus deck. The speed of the transition changes rapidly around 5°S as cumulus clouds develop more near the ITCZ, as shown in the low cloud fraction climatology. A number of factors play a role in where the minimum amount of clouds occurs along the trajectory, as the time it takes the transition from stratocumulus to cumulus may vary from year to year.

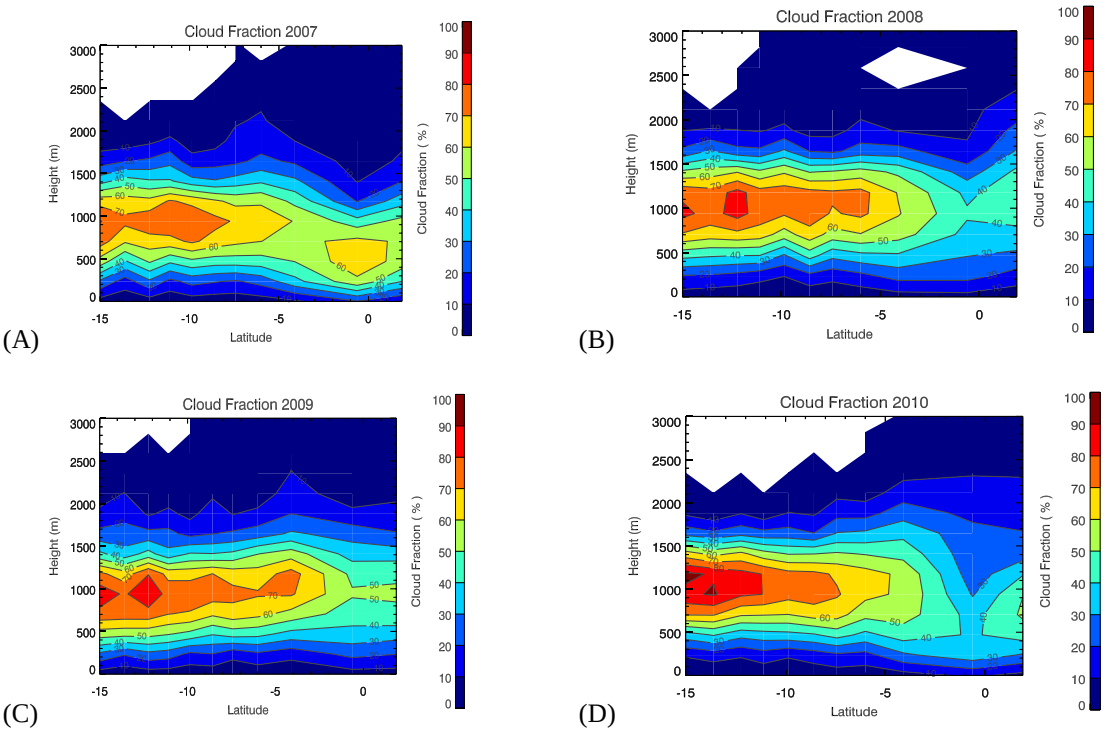

Figure 15: The cloud fraction (%) along the climatological wind trajectory in the southeast Pacific for (a) 2007, (b) 2008, (c) 2009, and (d) 2010.

The cloud layer top and base height in Figure 16 show that the mean height of the cloud top and base in 2007 are far lower just south of the equator when compared to the four-year mean and the other years. The SSTs in Figure 11 and temperature and moisture profiles shown in Figures 12 and 14 corroborate these findings, as a stronger temperature inversion and drier mid-troposphere is noted for both 2007 and 2010 in the southern latitudes, with 2007 indicating strong subsidence aloft inhibiting the typical vertical expansion of moisture and low SSTs with increased stability even near the equator.

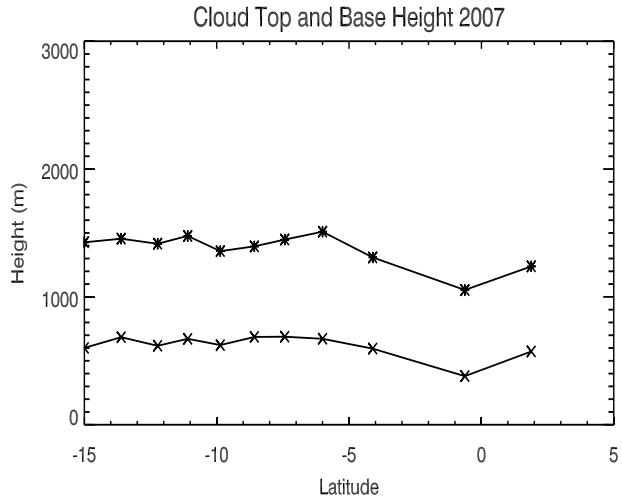

Figure 16: Cloud layer top and base heights (m) along the climatological wind trajectory in the southeast Pacific for 2007.

The LWP for non-precipitating clouds also display considerable variability from year to year and are compared to the four-year mean in Figure 17. LWP ranges by about 50 g m^{-2} in the southern latitudes and is largest in 2010 when the inversion and LTS is strongest. Mean LWP near the equator is also greater in 2010 as the cloud fraction transition occurs more rapidly and deeper clouds are more frequent. The large decrease in LWP in 2007 is likely false as many of the clouds between 6°S and the equator fall below the 720m limitation for CloudSat that inhibits the retrieval of cloud water content in the lower 2-3 bins.

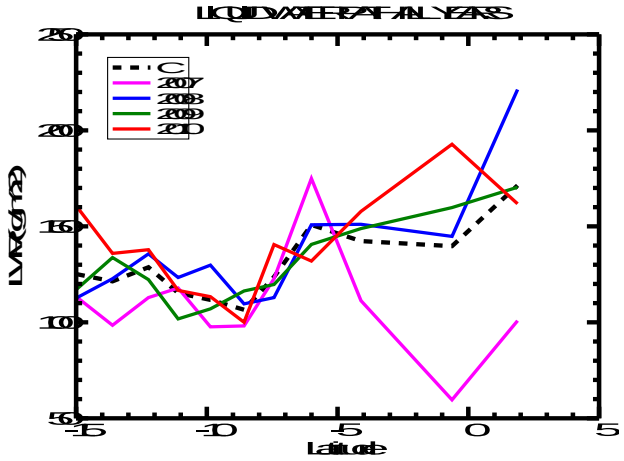

Figure 17: The LWP (g m^{-2}) for each year relative to the 4-year mean (black dashed) along the climatological wind trajectory in the southeast Pacific.

The interannual differences in the precipitation frequency is shown in Figure 18a and indicates yearly differences that scales with years on increased SST and decreased stability. The lowest frequency is in 2010, compared to 2009 where the rain frequency was generally the highest for all years. The year-to-year precipitation intensity in Figure 18b is lowest at 15 °S and overall increases as the trajectory approaches the equator. Near the equator light drizzle is less common as shallow cumulus produce more intense, convective rainfall. There is greater agreement in the southern portion of the study region, but the timing and location of the peak rain rates differ throughout the transition as 2009 and 2010 follow a similar pattern as the intensity increases during the transition from 8°S to the equator whereas 2007 and 2008 decrease over this portion of the trajectory. As the precipitation frequency decreases along the trajectory in 2007, it reaches a minimum near the equator, similar to that of the conditional rain rate, and the cloud base and top heights, although during this year the cloud fraction increased at the

equator, which did not occur in any other year. The subsidence and stability were also very strong throughout the trajectory for this year and the SSTs were much colder in 2007 near the equator. The beginning of the transition appears to occur when there is a peak in the rain rates in the southern portion of the region, however this timing differs for each year, with the transition occurring earliest in 2007.

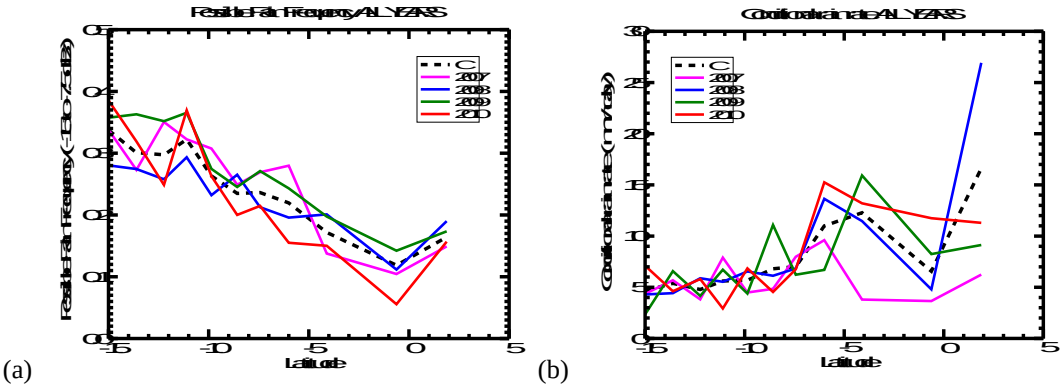

(a) (b)

Figure 18: The rain possible frequency (% likelihood) and conditional rain rate (mm day^{-1}) for cloud observations for each year relative to the 4-year mean climatology (black dashed).

The interannual variability along the trajectory for the longwave cooling in Figure 19 shows how each of the years are in general agreement with one another, although the year 2010 shows the greatest range as it is the strongest at 15 °S but weakest for all years at the equator. The gradual decrease is associated with the reduction of cloud cover, and dry, stable air.

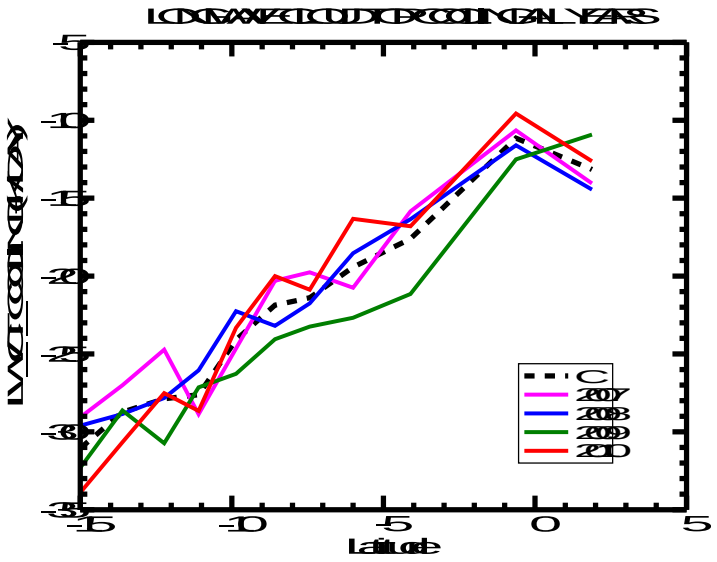

Figure 19: The longwave cooling rate (K d $^{-1}$) at the cloud top for each year relative to the 4-year mean climatology (black dashed)

3.3 Seasonal variability

Previous studies have shown considerably more variability from season to season than from year-to-year, as stratocumulus cloud cover is closely correlated with the SST and LTS cycle, which displays a significant seasonal cycle (Klein and Hartmann 1993; Wood and Bretherton 2006; Wood 2012). The intraseasonal variability is presented for several cloud, environmental, radiative, and precipitation variables to evaluate the differences across the transition from season-to-season. The seasons are represented by 3-month groups, labeled MAM, JJA, SON, and DJF.

The SST for each season is compared to the four-year mean in Figure 20, where values in MAM, JJA, and DJF are all significantly larger than the values in SON, particularly in the southern trajectory points. At 15°S, the SSTs are 5°C cooler in SON

compared to MAM. The temperature profiles for MAM and SON are compared in Figure 21a-b. DJF and MAM possess similar features and the JJA and SON are also very similar for the many of the variables and are omitted here for brevity. The largest difference between the two seasons is found in the southern portion of the study region where the temperature inversion is much stronger in SON than MAM. Temperatures are lower in the boundary layer in SON, which correlates to the lower SST values for SON. However, the temperatures in SON are greater above the boundary layer suggesting that enhanced subsidence is a major contributor to the stronger temperature inversion for these two seasons. The LTS for each season is compared to the four-year mean in Figure 22, where they all follow a similar trend to that of the four-year mean. The LTS for SON exhibits the most stability throughout the trajectory compared to all three of the other seasons, due to the much stronger inversion in place and cooler SSTs. The LTS and the SST shown in Figure 20 exhibit similar features because the two variables are inversely related, so as SSTs increase, the stability decreases. The specific humidity for MAM and SON are compared in Figure 23 a-b. Specific humidity is greater for MAM where values exceed 8 g kg^{-1} throughout much of the profile corresponding to the higher temperatures in MAM. For SON values below 8 g kg^{-1} are observed more frequently associated with the lower temperatures. Dry air aloft is found throughout the trajectory from the stronger subsidence during SON, suppressing the depth of the shallow moist layer along the trajectory.

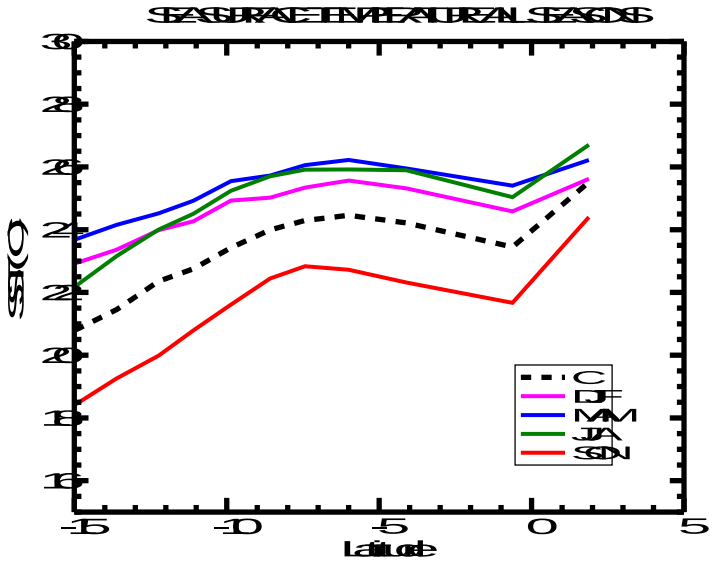

Figure 20: The SST (°C) along the climatological wind trajectory in the southeast Pacific for each season relative to the 4-year mean (black dashed).

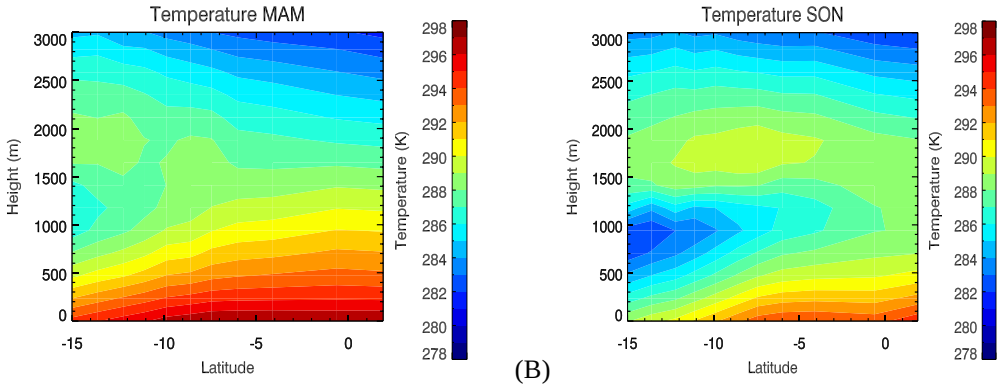

(A) (B)

Figure 21: The temperature profile (K) along the climatological wind trajectory in the southeast Pacific for both (a) MAM and (b) SON.

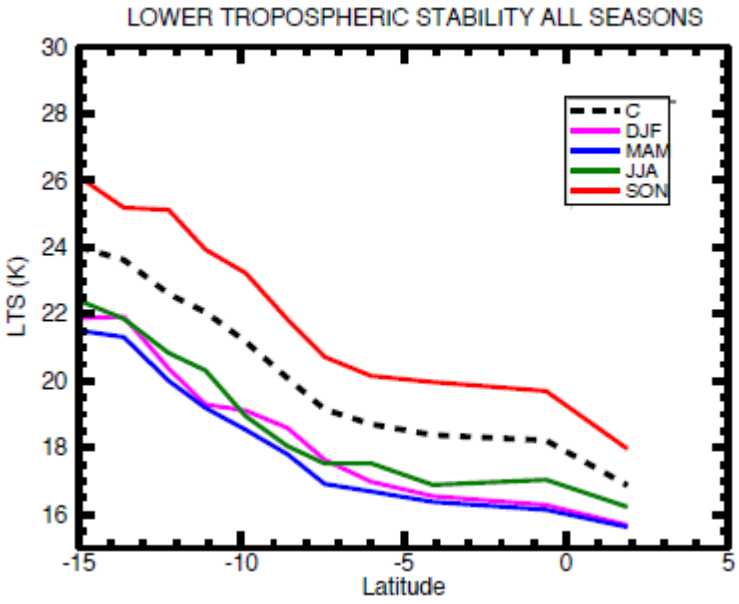

Figure 22: The LTS (K) along the climatological wind trajectory in the southeast Pacific for each season relative to the 4-year mean (black dashed).

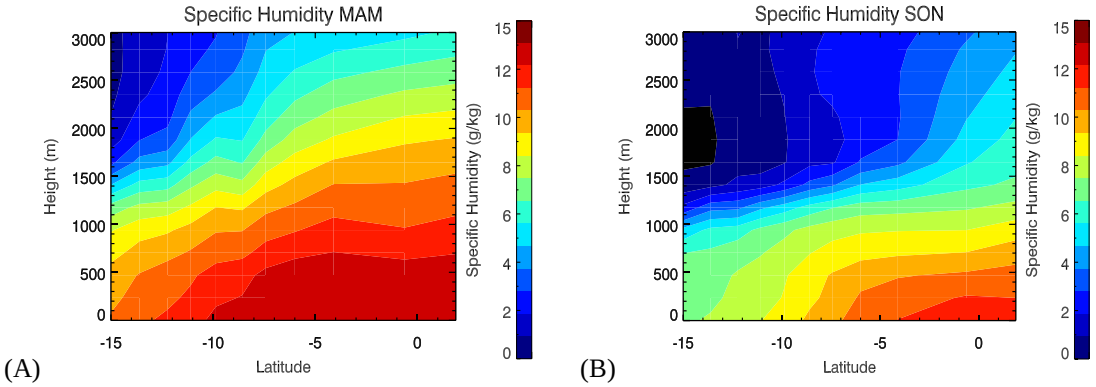

Figure 23: The specific humidity profile (g kg^{-1}) along the climatological wind trajectory in the southeast Pacific for both (a) MAM and (b) SON.

The cloud fraction for each of the four seasons varies considerably in Figure 24 a-d with much greater cloud fractions in SON compared to all other seasons throughout the boundary layer. The greatest cloud fractions for all seasons are found between 0.6 – 1.5 km; however, the maximum cloud fraction is between 1 – 1.5 km for DJF and MAM and is closer to 750 m for JJA and SON. The mean cloud top and base heights for MAM and SON are compared in Figure 25 a-b. The MAM season in Figure 25a shows higher values for both the base and the top of the cloud layer throughout the trajectory compared to the SON season in Figure 25b. The timing and speed of the transition differ between seasons, where the fastest transition occurs in MAM and DJF when the cloud cover over the southern boxes quickly declines along the trajectory. As the subtropical high develops during JJA, the timing of the transition is slower, although the slowest transition occurs in SON when the cloud fraction remains high throughout the trajectory and only declines slightly near the equator.

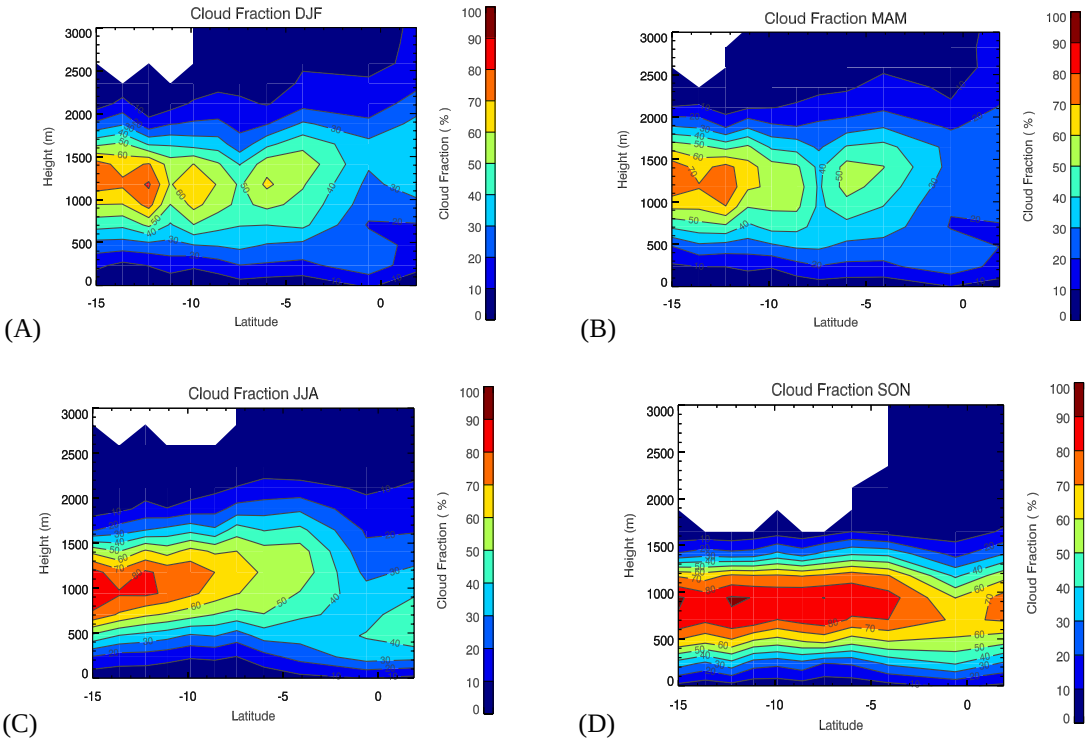

Figure 24: Cloud fraction (%) along the climatological wind trajectory in the southeast Pacific for (a) DJF, (b) MAM, (c) JJA, and (d) SON.

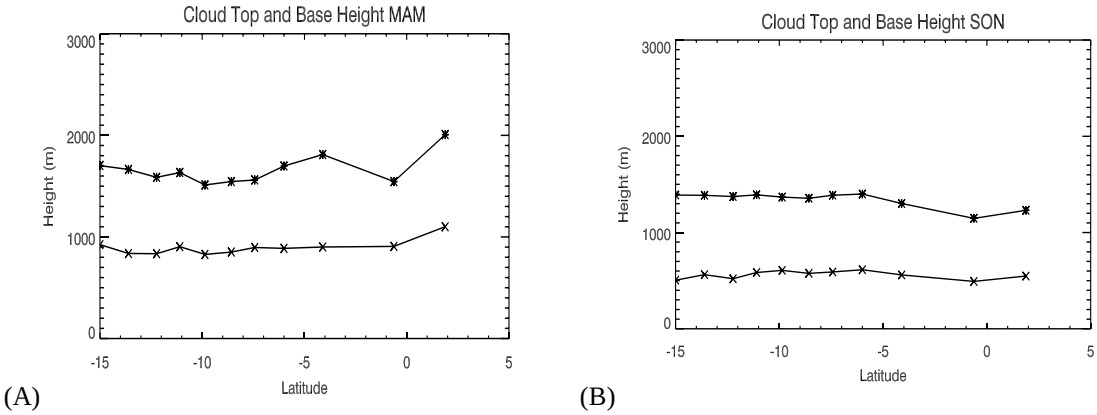

Figure 25: Cloud layer top and base height (m) along the climatological wind trajectory in the southeast Pacific for (A) MAM and (B) SON.

The LWP for non-precipitating clouds for each season is shown in Figure 26. The greatest values for LWP occur during MAM and DJF when there is a greater occurrence of deeper clouds, as shown by the higher cloud top heights denoted in Figure 25a and larger cloud fractions above 2 km throughout the trajectory, resulting in increased mean LWPs. The mean LWP in SON when clouds are most frequent, and thus the climatological mean, are likely drastically underestimated as much of the cloud detected during this season fall below 720 m and CloudSat is unable to distinguish them from ground clutter for the cloud property retrievals.

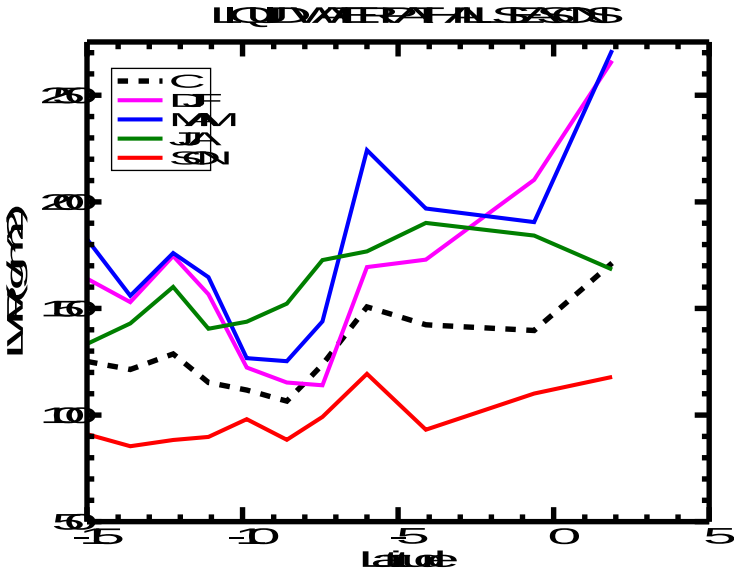

Figure 26: The LWP (g m^{-2}) for each season relative to the 4-year mean climatology (black dashed).

The rain possible frequency for cloud observations in Figure 27a is highest in JJA and SON and the variability between seasons is largest in the southern portion of the

domain where the cloud fraction is greatest. It is possible that some precipitation during SON is missed; however, Rapp et al. (2013) showed that the fraction of precipitating clouds with tops below 1km in this region obscured by CloudSat's ground clutter signal is likely less than 5%. For DJF and MAM, the rain frequency was lower throughout the trajectory but corresponds well to the observed changes in LWP and cloud fraction. The rainfall intensity for all seasons in Figure 27b is greatest for DJF and MAM and reaches a peak around 8°S; however this peak is potentially misleading as there are fewer precipitating clouds over this region in that period. On the other hand, if these higher rain rates are not an artifact of averaging fewer observations, it could potentially point to increased precipitation intensity playing a role in the rapid transition in cloud fraction observed in the same region during these months.

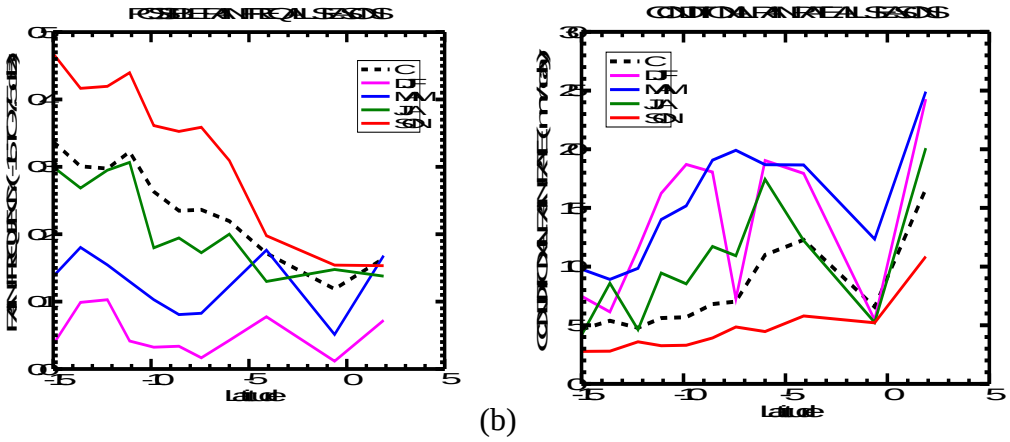

Figure 27: (a) The rain possible frequency (% likelihood) and (b) the conditional rain rate (mm day^{-1}) of cloud observations for each season relative to the 4-year mean climatology (black dashed).

The seasonal shortwave TOA_CRE is compared for all scenes in Figure 28. A much weaker cloud radiative effect is found for MAM compared to SON south of the equator, especially close to 15°S where over a 100 Wm^{-2} difference between the two seasons is observed. However, values are much more similar from season to season near the equator. The weaker cloud radiative effect is a result of smaller cloud fractions in MAM compared to SON. The longwave cloud top cooling for all seasons are compared to the four-year mean in Figure 29 where there is a weaker gradient for DJF/MAM and the values are usually smaller than SON, indicating less turbulence and coupling with the surface.

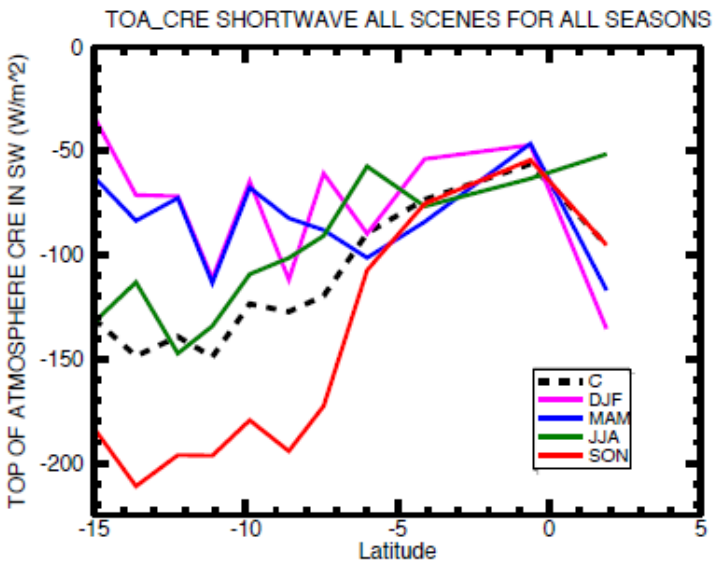

Figure 28: The TOA shortwave cloud radiative effect (W m^{-2}) for each season relative to the 4-year mean climatology (black dashed).

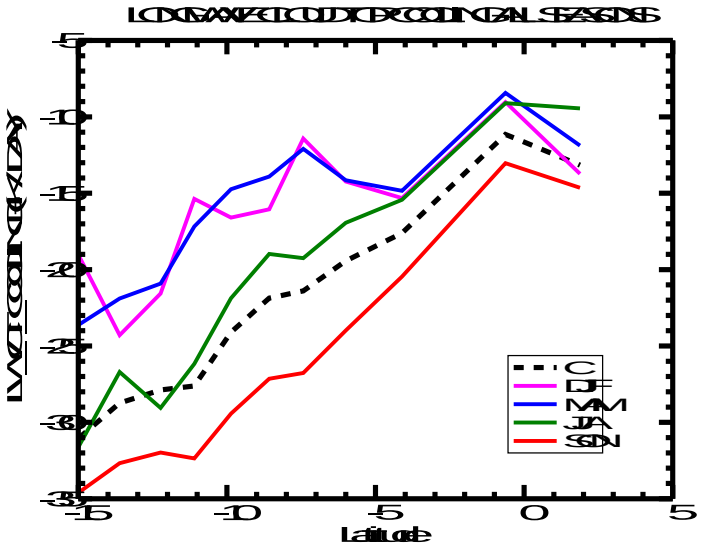

Figure 29: The longwave cloud top cooling rate (K d^{-1}) for each season compared to the 4-year mean climatology (black dashed).

Clouds are more frequent and more shallow in JJA and SON compared to MAM and DJF, where deeper clouds occur more frequently. The LWP is also higher for DJF and MAM north of the equator where both the precipitation frequency and rain rates increase dramatically. The cold SSTs, strong temperature inversion, and strong subsidence found during SON impact the height of the cloud layer by creating a strong capping inversion, thus a persistent deck of lower clouds is observed, contributing to the greater precipitation frequency and strong cloud radiative effect in the shortwave and strong longwave cooling in the southern boxes of the trajectory before the transition occurs. The transition appears to occur faster in DJF and MAM where more intense rainfall may help to speed up the process by depleting the cloud layer as environmental conditions are not as favorable for stratocumulus cloud development and the TOA_CRE

and longwave cooling are much weaker as a result. Therefore, the environmental conditions in place for each season and the potential feedback of precipitation greatly impact the clouds, as well as timing of the transition to shallow cumulus clouds.

3.4 Diurnal variability

Stratocumulus clouds have been shown in numerous studies to exhibit strong diurnal effects (Hignett 1991; Miller et al. 1998; Wood 2012). Variables important for the observed diurnal cycle in these clouds will be highlighted in this section to show their day-to-night differences. It should be noted that these results do not represent the full diurnal cycle. Instead, they represent the day/night differences between observations at the two CloudSat overpass times.

The temperature profile for day and night in Figure 30 a-b displays warmer temperatures during the day, as expected, and the inversion, though not much stronger, expands toward the equator at night compared to the daytime. Past studies have shown that the temperature inversion is considerably stronger at night than in the daytime (Caldwell et al. 2005). The poor vertical resolution of the ECMWF analysis data used in this study likely results in the lack of significant strengthening overnight compared to other in situ studies. Similar results are evident in the other environmental variables; therefore, they are omitted here for brevity.

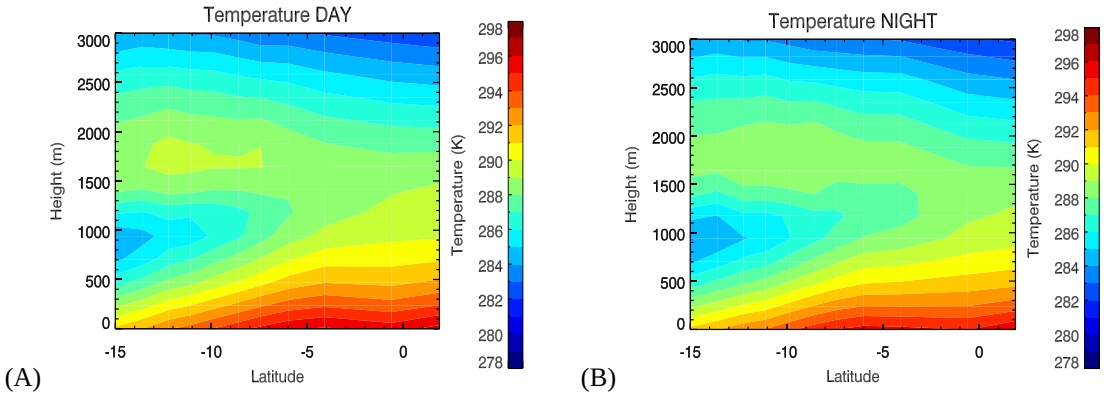

(A) (B)

Figure 30: The temperature profiles (K) for (A) day and (B) night.

Figure 31 a-b displays the daytime and nighttime plots for the vertical profile of cloud fraction. Overall, there is much greater cloud fraction in the overnight hours compared to the daytime. During the day, the clouds absorb solar radiation and begin to break up, consistent with the results in Miller et al. (1998). Figure 32 shows the comparison of the height of the top and base of the single cloud layer in the day and at night. During the daytime overpasses, cloud layer tops remain fairly constant around 1.4 km and the base of the single cloud layer also remain fairly constant around 0.8 km. During the nighttime overpasses, cloud layer top heights range from 1.4 – 1.6 km and the cloud layer base heights remain fairly constant around 0.6 km. Therefore, the cloud layer deepens at all locations along the trajectory at night compared to the daytime. Again, solar absorption weakens the circulations and the efficient coupling with the surface that promote the cloud develop overnight (Hignett 1991; Miller et al. 1998; Caldwell et al 2005; Wood 2012). The LWP values for daytime and nighttime trajectory points are displayed in Figure 33. LWP values are always higher at night when clouds are more frequent than during the day. The larger LWP at night may be due to several

factors such as the greater subsidence, and longwave cooling at the cloud top that drive the turbulence in the cloud layer. The cloud layer is also deeper at night than during the day, which corresponds to the increased LWP values and cloud fraction.

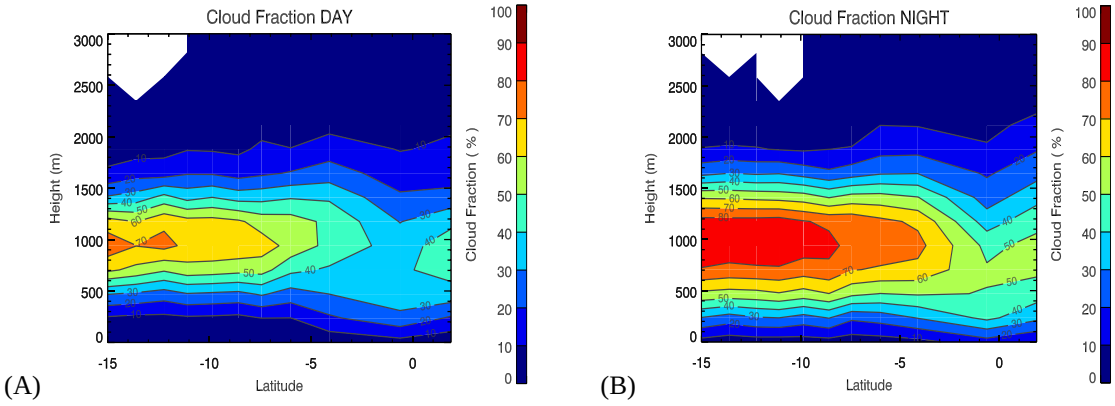

Figure 31: The cloud fraction (%) along the climatological wind trajectory in the southeast Pacific for (A) daytime overpasses and (B) nighttime overpasses.

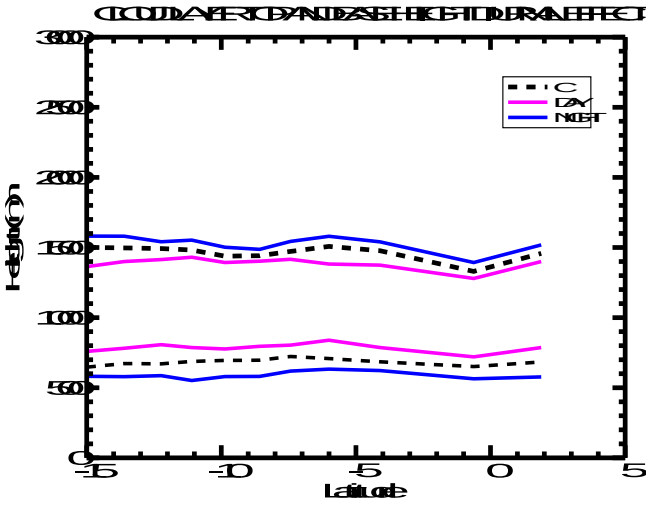

Figure 32: The cloud layer top and base heights (m) for day (pink) and night (blue).

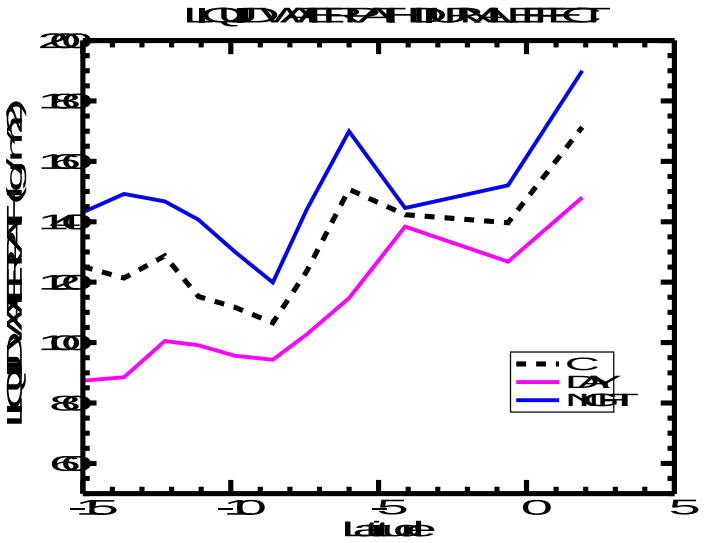

Figure 33: The LWP (g m^{-2}) for day (pink) and night (blue).

The rain frequency for cloud observations is compared in Figure 34 a-b, where rain frequency is higher at night. For the daytime (Figure 34a), generally rain is less frequent, which is consistent with the reduced cloud fraction and LWP during the day. The cloud layer is also thinner in the daytime compared to the nighttime, likely in part due to the precipitation that helps deplete the cloud layer during the early morning hours. The conditional rain rate is compared in Figure 35 a-b, where rain rates are generally greater during the day when more convection is present compared to at night. The peak around 4°S in Figure 35b corresponds to the reduction in cloud cover in Figure 31b as clouds begin to break up faster due to the depletion of the cloud layer from the higher rainfall intensity. The sudden dip in rainfall intensity is due to the lack of convection and cloud cover over the equator.

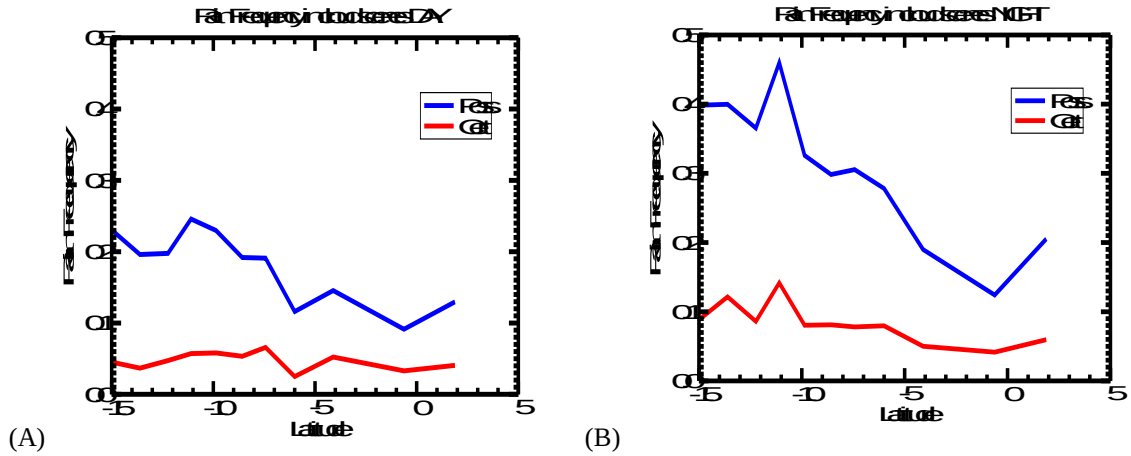

(A) (B)

Figure 34: The rain possible frequency (blue) and the rain certain frequency (red) for (A) day and (B) night.

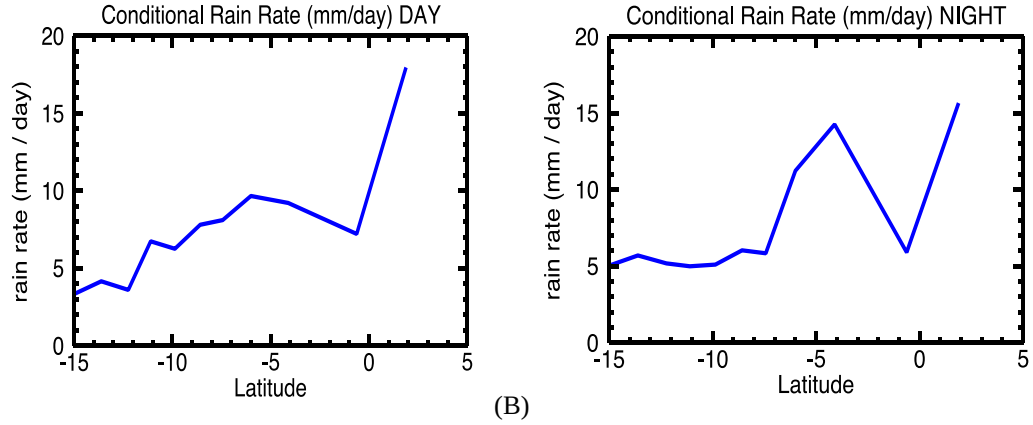

(A) (B)

Figure 35: The conditional rain rates (mm d^{-1}) for (A) day and (B) night.

Comparing the daytime and nighttime cloud top longwave cooling, lower values are present in Figure 36 throughout the trajectory during the nighttime hours relative to the daytime hours. The enhanced longwave radiative cooling in the overnight hours leads to more low-level instability and results in stronger turbulence (Tutron and Nicholls 1987; Rogers and Koracin 1992; Miller et al. 1998; Wood 2012).

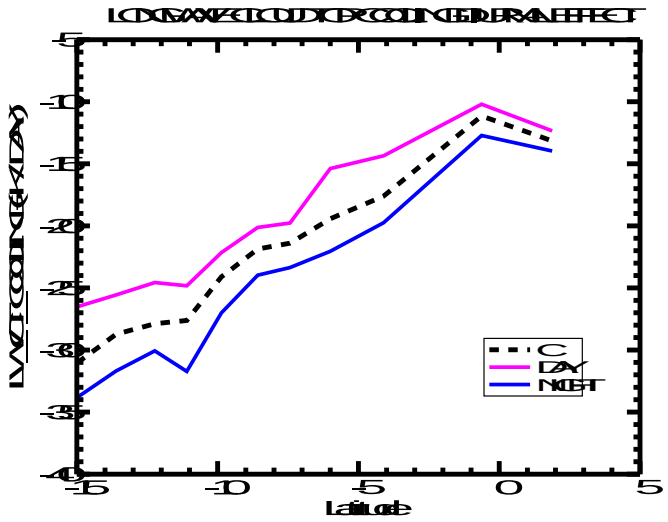

Figure 36: The longwave cloud top cooling (K d^{-1}) for day (pink) and night (blue).

At night, the enhanced longwave cooling acts to drive the turbulence within the boundary layer, coupling the cloud layer with the surface and increasing the cloud fraction. This process occurs throughout the trajectory, even in regions where conditions are less favorable for stratocumulus cloud development, or where SSTs are warmer or the LTS is weaker. As the clouds thicken, the likelihood of precipitation increases, with the precipitation frequency reaching a peak in the early morning hours just before sunrise (Comstock et al. 2005), though this may act to further deplete the cloud layer during the day and speed up the transition process. Conditions change during the day as the shortwave heating rates (not shown) act to dampen the effect of longwave cooling on the clouds, causing a reduction in cloud cover and thickness as the cloud begins to decouple and dissipate with the decrease in turbulence. In regions closer to the equator where the cloud fraction is lower overnight, the transition to shallow cumulus occurs

faster during the day as the region responds quicker to the daytime heating and leads to unfavorable conditions for stratocumulus cloud development.

4. SUMMARY AND DISCUSSION

4.1 Summary

In this thesis the environmental, cloud, precipitation, and radiative characteristics of stratocumulus clouds were investigated as they transition into shallow cumulus clouds over the southeast Pacific Ocean from 2006 – 2010. This study was motivated by new CloudSat and CALIPSO measurements that help bridge some of the gaps due to limitations in existing satellite measurements and the lack of long-term *in situ* studies on this transition.

Analysis of satellite measurements along the climatological wind trajectory in the southeast Pacific Ocean showed that as trade winds advect toward the equator from the Peruvian coastline, thick, persistent, low-level stratocumulus clouds with high cloud fractions gradually transition to shallow cumulus with lower cloud fractions. The climatological transition in mean cloud fraction in Figure 8f is similar to the MODIS results in Sandu et al (2010). The conclusion of the transition period, or where the minimum cloud fraction is observed along the trajectory, depends greatly on the environmental conditions as the speed at which the clouds transitioned from marine stratocumulus to shallow cumulus clouds varies interannually. The average change in cloud fraction between the peak and minimum in cloud fraction varies considerably along the trajectory each year as 2010 represented a much quicker transition whereas 2007 experienced a longer transition where the minimum in cloud fraction was observed further north along the trajectory. In addition to mean cloud fraction, this thesis also

explored other cloud parameters such as the vertical profile of cloud fraction, cloud height/thickness, cloud LWP, and the effective radius.

In the southernmost part of the trajectory, strong subsidence, temperature inversions, and LTS above the lower SSTs, along with the enhanced cloud top longwave cooling drives the turbulence within the boundary layer to increase the cloud fraction and cloud thickness. These conditions are also the most favorable for the onset of precipitation. Closer to the equator, SSTs increase and the temperature inversion, LTS, and the longwave cooling at the cloud top are weaker, suggesting reduced turbulence, and less frequent coupling with the surface, which is necessary to maintain the large stratocumulus decks. LWP and effective radius each increase as deeper clouds occur more frequently as the trajectory approaches the equator.

Precipitation is most frequent in the southern portion of the study region where strong subsidence, higher longwave cooling rates, cool SSTs, and a strong temperature inversion are in place to generate and maintain thick, low-level clouds. As the cloud cover declines, precipitation frequency also declines, but the intensity of rainfall increases as there more frequent deeper clouds with higher LWPs suggesting the transition to more convective rainfall in shallow cumulus. The impact of the transition from marine stratocumulus to shallow cumulus on the top of atmosphere energy budget is also illustrated through the shortwave TOA_CRE, which decreases with the cloud fraction as trade winds advected toward the equator

Examination of the interannual variability in the transition showed that the temperature inversion and LTS was stronger in 2010 compared to other years especially

in the southern portion of the study domain, likely due to the enhanced dry subsiding air above the boundary layer, which resulted in the highest cloud fractions in the study period. However, these conditions change rapidly with the onset of the transition over warmer SSTs, although the timing for the transition is different each year. The strength of the equatorial cold tongue in SST also appears to play an important role in the interannual differences in the timing of transition.

Intraseasonal comparisons across the transition show that conditions for cloud development are most favorable in the austral spring and winter, or JJA and SON, evidenced by the increased cloud fraction, which results in stronger cloud top longwave cooling to drive the turbulence that more efficiently couples the clouds with the surface. This seasonal increase in cloud fraction is consistent with many previous studies (Klein and Hartmann, 1993; Norris et al. 1998; Lin et al. 2009). The LWP featured considerable seasonal variability across the entire trajectory, but especially closer to the equator where values ranged from over 250 gm^{-2} in MAM and DJF to about 100 gm^{-2} in SON. Cloud fraction results indicate a much slower transition during SON, with stratocumulus dominating even near the equator, leading to the observed seasonal differences in LWP. The conditional rain rates during MAM and DJF show the highest rainfall intensity throughout the trajectory. While this could be an artifact of the less frequent precipitation occurrence, it could also be why the LWP and total cloud fraction each decrease dramatically in the region of the rain rate increases, since this may increase the rate at which the cloud is depleted (Comstock et al. 2005; Stevens et al. 2005).

A strong diurnal cycle is detected in the findings presented here, as clouds and precipitation occur more frequently at night than during the day. The characteristics of clouds change overnight as clouds thicken and grow in number under the stronger longwave cooling rates at the cloud top and enhanced turbulence within the cloud. The lack of solar absorption at night increases the cooling rate at the cloud top, which allows the moisture within the cloud to build up and increase the cloud heights by the lowering of the cloud base and rise in the cloud top, increasing the likelihood of precipitation.

4.2 Discussion

Analysis of the characteristics of clouds as they transition from stratocumulus to shallow cumulus clouds, suggests significant interannual, intraseasonal, and diurnal variability in the transition over the southeast Pacific.

The impact of ENSO is felt in several ways over the study region, particularly on the SSTs and the strength of the Walker circulation (Julian and Chervin 1978; Rassmuson and Wallace 1983). Two El Niño events took place in the beginning of 2007 and 2010, with the 2007 event considered a moderate eastern Pacific El Niño and the latter a much stronger central El Niño event (Su and Jiang 2013). Both years rapidly transitioned to La Niña conditions during austral winter and spring when cloud fractions were greatest. For 2007, the SSTs were much lower than other years over the equatorial cold tongue suggesting an enhanced cold tongue as the moderate eastern Pacific El Niño switched to La Niña conditions during the latter half of the year. In 2010, the SST was still lower than 2008 and 2009, but not to the extent of 2007. This resulted in a slower

transition in 2007 as clouds continued to develop under the dry stable air and above the cooler SSTs near the equator. The transition occurs more rapidly when SSTs are warmer, suggesting that the SST gradient plays a major role in the timing of the transition. The different timing of the transitions for each year may pose a significant problem for climate models because of the characteristics like SST and subsidence strength that drive the features of the clouds as they transition from stratocumulus to shallow cumulus. Teixeira et al. (2011) found that climate models have difficulties in accurately timing the beginning and the speed of the transition, as many models transition too early compared to observations, leading to an underestimation of clouds in the transition. It is important that climate models improve the characterization of this transition, as the cloud-climate feedback depends heavily on the relative contributions of stratocumulus and shallow cumulus to the cloud fraction and property distributions. The results here suggest that it is important for models to capture these differences in the transitions due to changes in the large-scale circulation associated with El Niño and La Niña events.

Previous studies (Zhang et al. 2005; Rapp 2014) suggest that climate models are unable to accurately simulate the seasonal cycle of low clouds in subsidence regimes even in uncoupled models. The results presented here show large seasonal variability in cloud variables and in the timing of the transition, where a faster transition occurs in seasons where SSTs are warmer and the gradient is weaker, while the opposite occurs when SSTs are cooler and the gradient is strong. This suggests that capturing the seasonal variability in these transitions may play an important role in improving the low cloud response in climate models. Several studies have shown that coupled atmosphere-

ocean models display difficulty in accurately simulating SSTs over this complex region, with a cold bias along the equatorial Pacific region and a warm bias closer to the coast of Peru where models fail to produce the coastal upwelling (Ma et al. 1996; Kiehl and Gent 2004; Wittenberg et al. 2006). Thus the intraseasonal findings presented here suggest a positive feedback in models that are unable to accurately capture the transitions and SSTs throughout the seasonal cycle. For instance, in models with a positive SST bias and transitions that are too rapid, the SSTs will further increase, resulting in an even faster transition because of the rapidly weakening longwave cooling rate and reduction of cloud cover. The weaker longwave cooling rate and reduction in cloud cover will weaken the shortwave cloud radiative effect at the top of the atmosphere, because of the lack of thick cloud cover and will further increase the SSTs, adding to the model error.

The onset of precipitation plays an important role in the transition process through the development of open cells in areas where the rain rate is higher (Comstock et al. 2005; Stevens et al. 2005). Results presented here and in previous studies (Austin et al. 1995; Stevens et al. 2003; Comstock et al. 2005) found depleted the cloud amount and cloud liquid water path in regions of precipitation and that drizzling regimes correspond to increased variability of cloud and boundary layer properties (Comstock et al. 2005). In regions and seasons where the rainfall intensity was higher, similar to the strong drizzle events observed during the ASTEX campaign in the northeast Atlantic (Albrecht et al 1995), lower cloud fractions were observed in this study during the transition in DJF and MAM. While these higher rain rates may in part be due to fewer observations in the calculation of the mean, these two seasons also showed earlier

transitions than JJA and SON, and suggest that the greater rainfall intensity may result in a quicker depletion of the cloud layer and development of the open-celled cloud patterns, as discussed by Stevens et al. (2005). However, climate models have difficulty accurately simulating the occurrence and intensity of precipitation in low clouds. Siebesma et al. (2004) found that when there is an excessive amount of drizzle, models tend to underestimate cloud amount, which suggests that capturing the feedbacks of both precipitation frequency and intensity for the cloud layer is necessary for improving model simulations of the transition from stratocumulus to shallow cumulus.

Marine boundary layer stratocumulus and shallow cumulus clouds pose a major problem for current climate models. Bony and Dufresne (2005) found that in regions of large-scale subsidence, the radiative response of low-level clouds to a change in temperature shows the largest differences among models in climate change and also disagrees most with the observations. Therefore low-level clouds pose the greatest uncertainty for climate model cloud feedbacks. Similar to previous studies (Bony and Dufresne 2005), the results here show that the shortwave TOA_CRE is greatest in areas of stronger subsidence and lower SSTs, but as SSTs increases a reduction in cloud cover across the transition leads to a weaker shortwave TOA_CRE. However, models have large uncertainties the shortwave TOA_CRE and their response to temperature, likely due in part to the inability of climate models to accurately capture the seasonal variability in the transition from marine stratocumulus to shallow cumulus clouds (Bony and Dufresne 2005; Rapp 2014). The results in this thesis suggest that until they are able to better capture the variability in these transitions, models will have difficulty

simulating the sensitivity of these clouds to the evolving environmental conditions.

4.3 Limitations

The findings presented here have several limitations, which include but are not limited to, contamination of measurements by CloudSat's CPR below 750m due to ground clutter, the nadir-only sampling of CloudSat, allowing only a statistical analysis over a large number of observation, as well as several problems with some of the CloudSat cloud retrieval products that limit our analysis of some cloud variables to observations without precipitation. However, the mean patterns of the transition in cloud variables are not expected to differ significantly since precipitation is relatively infrequent and lower in intensity. Although the addition of CALIPSO captures cloud that falls below 750m, yielding higher quality cloud fraction observations, there is the possibility that some of the CloudSat retrieved cloud properties, like LWP, are biased since the lower portion of the cloud is not observed, which may result in a poor representation of the mean cloud properties. The largest impacts on the cloud properties will occur in the austral spring months when cloud bases are lowest or during events like the 2007 shift from El Niño to La Niña when the clouds were much lower over the anomalously low SSTs in the equatorial cold tongue.

Another potential issue that should be addressed is related to the method in which observations were aggregated in this study due to the limited sampling of CloudSat, which does not allow for a Lagrangian analysis of the actual three-day transition. The main assumption here is that the climatological trajectory is highly

representative of transition processes that occur during a typical three-day transition. However, using the climatological trajectory instead of a single actual trajectory may lead to important localized features that occur during the transition being missed completely, especially if the speed or locations of these processes are slightly different than the mean.

4.4 Future Work

Although this study touched on several components of the stratocumulus to shallow cumulus transition, a number of topics still need to be addressed. While briefly mentioned in this discussion, the two El Niño events discussed in Su and Jiang (2013) that occurred during this study period could be further analyzed by performing an in-depth comparison of during DJF peak months of the 2006/2007 and 2009/2010 events. Analysis of an additional dataset like MODIS for the cloud properties would also be beneficial in augmenting some of the shortcomings of the new CloudSat retrievals mentioned in the previous section, although this would be limited to daytime scenes only. Finally, and of upmost importance, to better understand the limitations and further improve the representation of the stratocumulus to shallow cumulus transition in current climate models, the results from this study should be compared to the transitions found in reanalysis data and simulated by climate models over the study region.

5. CONCLUSIONS

For this study, observations from CloudSat and CALIPSO showed that clouds are most persistent with the strongest cloud radiative effects in the southern portion of the study region, where a strong temperature inversion and warm, dry subsiding air over a cool, moist boundary provide the stability necessary to maintain the stratocumulus. As the trade winds advect equatorward, clouds and their radiative effects decrease as they transition to shallow cumulus in the regions of a weakened temperature inversion, less subsidence, greater rainfall rates, and higher SSTs. The speed of this transition exhibits considerable interannual, seasonal, and diurnal differences associated with changes in the large-scale environment. Capturing the variability in these transitions is a major concern to climate modelers, as models are currently unable to accurately capture the speed and timing of the transition.

REFERENCES

Albrecht, B. A., M. P. Jensen, and W. J. Syrett 1995: Marine boundary layer structure and fractional cloudiness, *J. Geophys. Res.*, **100**, 14209–14222, doi:10.1029/95JD00827.

Austin, P., Y. Wang, V. Kujala, and R. Pincus, 1995: Precipitation in stratocumulus clouds: observational and modeling results. *J. Atmos. Sci.*, **52**, 2329–2352, doi: http://dx.doi.org/10.1175/1520-0469(1995)052<2329:PISCOA>2.0.CO;2

Austin, R. T., and G. L. Stephens, 2001: Retrieval of stratus cloud microphysical parameters using millimeter-wave radar and visible optical depth in preparation for CloudSat: 1. Algorithm formulation, *J. Geophys. Res.*, **106**, 28233–28242, doi:10.1029/2000JD000293.

Barker, H. W., A. V. Korolev, D. R. Hudak, J. W. Strapp, K. B. Strawbridge, and M. Wolde, 2008: A comparison between CloudSat and aircraft data for a multilayer, mixed phase cloud system during the Canadian CloudSat-CALIPSO Validation Project, *J. Geophys. Res*., **113**, D00A16, doi:10.1029/2008JD009971.

Bodhaine, B. A., N. B. Wood, E. G. Dutton, and J. R. Slusser, 1999: On rayleigh optical depth calculations. *J. Atmos. Oceanic Technol.*, **16**, 1854–1861, doi: http://dx.doi.org.lib-ezproxy.tamu.edu:2048/10.1175/1520-0426(1999)016<1854:ORODC>2.0.CO;2

Bony, S., and J.L. Dufresne, 2005: Marine boundary layer clouds at the heart of tropical cloud feedback uncertainties in climate models. *Geophys. Res. Lett.*, **32**, L20806, doi:10.1029/2005GL023851

Bretherton, C. S., and M. C., Wyant, 1997: Moisture transport, lower-tropospheric stability, and decoupling of cloud-topped boundary layers. *J. Atmos. Sci.*, **54**, 148–167.

Bretherton, C. S., and Coauthors, 2004: The Epic 2001 stratocumulus study. *Bull. Amer. Meteor. Soc.*, **85**, 967–977, doi: http://dx.doi.org/10.1175/BAMS-85-7-967.

Bretherton, C. S., R. Wood, R. C. George, D. Leon, G. Allen, and X. Zheng, 2010: Southeast Pacific stratocumulus clouds, precipitation and boundary layer structure sampled along 20° S during VOCALS-REx, *Atmos. Chem. Phys*., **10**, 10639-10654, doi:10.5194/acp-10-10639-2010.

Caldwell, Peter, C. S. Bretherton, and R. Wood, 2005: Mixed-layer budget analysis of the diurnal cycle of entrainment in southeast Pacific stratocumulus. *J. Atmos. Sci.*, **62**, 3775–3791.

Charlock, T. P. and V. Ramanathan, 1985: The albedo field and cloud radiative forcing produced by a general circulation model with internally generated cloud optics, *J. Atmos. Sci*., **42**, 1408–1429.

Cheng, A., and K. M. Xu, 2013: Evaluating low-cloud simulation from an upgraded multiscale modeling framework model. Part III: Tropical and subtropical cloud transitions over the northern Pacific. *J. Climate*, **26**, 5761–5781, doi: http://dx.doi.org/10.1175/JCLI-D-12-00650.1

Christensen, M. W., G. G. Carrió, G. L. Stephens, and W. R. Cotton, 2013: Radiative impacts of free-tropospheric clouds on the properties of marine stratocumulus. *J. Atmos. Sci.*, **70**, 3102–3118.

Chung, D., and J. Teixeira, 2012: A simple model for stratocumulus to shallow cumulus cloud transitions. *J. Climate*, **25**, 2547–2554, doi: http://dx.doi.org/10.1175/JCLI-D-11-00105.1

Chung, D., G. Matheou, and J. Teixeira, 2012: Steady-state large-eddy simulations to study the stratocumulus to shallow cumulus cloud transition. *J.Atmos.Sci.*, **69**, 3264–3276, doi: http://dx.doi.org/10.1175/JAS-D-11-0256.1

Comstock, K., C. S. Bretherton, and S. Yuter, 2005: Mesoscale variability and drizzle in southeast Pacific stratocumulus. *J. Atmos. Sci.*, **62**, 3792–3807.

Comstock, K. K., R. Wood, S. E. Yuter, and C. S. Bretherton, 2004: Reflectivity and rain rate in and below drizzling stratocumulus. *Q.J.R. Meteorol. Soc.*, **130,** 2891–918.

Deng, W., T. L. Killeen, A. G. Burns, R. M. Johnson, B. A. Emery, R. G. Roble, J. D. Winningham, and J. B. Gary, 1995: One-dimensional hybrid satellite track model for the Dynamics Explorer 2 (DE 2) satellite, *J. Geophys. Res.*, **100**, 1611–1624, doi:10.1029/94JA02075.

de Szoeke, S. P., Y. Wang, S. P. Xie, and T. Miyama, 2006: Effect of shallow cumulus convection on the eastern Pacific climate in a coupled model. *Geophys. Res. Lett.*, **33**, L17713, doi:10.1029/2006GL026715.

Devasthale, A., and M. A. Thomas, 2012: Sensitivity of cloud liquid water content estimates to the temperature-dependent thermodynamic phase: A global study using CloudSat data. *J. Climate*, **25**, 7297–7307.

Dufresne, J. L., and S. Bony, 2008: An assessment of the primary sources of spread of global warming estimates from coupled atmosphere-ocean models. *Journal of Climate,* **21**, 5135-5144.

Duynkerke, P. G., and Coauthors, 2004: Observations and numerical simulations of the diurnal cycle of the EUROCS stratocumulus case. *Q.J.R. Meteorol. Soc.,* **130**: 3269–3296, doi: 10.1256/qj.03.139.

Garreaud, R. D., and R. Muñoz, 2004: The diurnal cycle in circulation and cloudiness over the subtropical southeast Pacific: A modeling study. *J. Climate*, **17**, 1699–1710,doi: http://dx.doi.org/10.1175/1520-0442(2004)017 <1699:TDCICA>2.0.CO;2.

Hamada, A., N.Nishi, 2010: Development of a cloud-top height estimation method by geostationary satellite split-window measurements trained with CloudSat data. *J. Appl. Meteor. Climatol.*, **49**, 2035–2049, doi: http://dx.doi.org/10.1175/2010JAMC2287.1

Hartmann, D. L., 1986: Earth radiation budget data and climate research, *Review of Geophysics*, **24**, 439-486.

Hartmann, D. L., 1994: *Global Physical Climatology*, 411 pp., Academic, New York.

Hartmann, D. L., M. E. Ockert-Bell, and M. L. Michelsen, 1992: The effect of cloud type on Earth's energy balance: global analysis. *J. Climate*, **5**, 1281–1304, doi: http://dx.doi.org/10.1175/1520-0442(1992)005<1281:TEOCTO>2.0.CO;2

Haynes, J. M., and G. L. Stephens, 2007: Tropical ocean cloudiness and the incidence of precipitation: Early results from CloudSat. *Geophys. Res. Lett.*, **34**, doi: 10.1029/2007GL029335.

Haynes J. M., T. S. L'Ecuyer, G. L. Stephens, S. D. Miller, C. Mitrescu, N. B. Wood and S. Tanelli, 2009: Rainfall retrieval over the ocean with spaceborne W-band radar *J. Geophys. Res.* **114,** D00A22

Hignett, P., 1991: Observations of diurnal variation in a cloud-capped marine boundary layer. *J. Atmos. Sci.*, **48**, 1474–1482.

Jensen, M. P., A. M. Vogelmann, W. D. Collins, G. J. Zhang, and E. P. Luke, 2008: Investigation of regional and seasonal variations in marine boundary layer cloud properties from MODIS observations. *J. Climate*, **21**, 4955-4973.

Julian, P. R., and R. M. Chervin, 1978: A study of the southern oscillation and walker circulation phenomenon. *Mon. Wea. Rev.*, **106**, 1433–1451, doi: http://dx.doi.org/10.1175/1520-0493(1978)106<1433:ASOTSO>2.0.CO;2

Kiehl, J. T., and P. R. Gent, 2004: The community climate system model, Version 2. *J. Climate*, **17**, 3666–3682.

Kim, M. J., M. S. Kulie, C. O'Dell, and R. Bennartz, 2007: Scattering of ice particles at microwave frequencies: A physically based parameterization. *J. Appl. Meteor. Climatol.*, **46**, 615–633.

Klein, S. A., and D. L. Hartmann, 1993: The seasonal cycle of low stratiform clouds. *J. Climate*, **6**, 1587–1606, doi: http://dx.doi.org/10.1175/1520-0442(1993)006<1587:TSCOLS>2.0.CO;2

Klein, Stephen A., Dennis L. Hartmann, Joel R. Norris, 1995: On the relationships among low-cloud structure, sea surface temperature, and atmospheric circulation in the summertime northeast Pacific. *J. Climate*, **8**, 1140–1155, doi: http://dx.doi.org/10.1175/1520-0442(1995)008<1140:OTRALC>2.0.CO;2

Kollias, P., C. W. Fairall, P. Zuidema, J. Tomlinson, and G. A. Wick, 2004: Observations of marine stratocumulus in SE Pacific during the PACS 2003 cruise, *Geophys. Res. Lett.*, **31**, L22110, doi:10.1029/2004GL020751.

Krueger, S. K., G. T. McLean, and Q. Fu, 1995: Numerical simulation of the stratus -to-cumulus transition in the Subtropical Marine Boundary Layer. Part I: Boundary-Layer Structure. *J. Atmos. Sci.*, **52**, 2839–2850, doi: http://dx.doi.org/10.1175/1520-0469(1995)052 <2839:NSOTST>2.0.CO;2

Kummerow, C., Y. Hong, W. S. Olson, S. Yang, R. F. Adler, J. McCollum, and T. T. Wilheit, 2001: The evolution of the goddard profiling algorithm (GPROF) for rainfall estimation from passive microwave sensors. *Journal of Applied Meteorology*, **40**, 1801-1820.

Lebsock, M. D., Stephens, G. L., and Kummerow, C., 2008: Multisensor satellite observations of aerosol effects on warm clouds. *J. Geophys. Res.: Atmospheres (1984–2012)*, **113**.

Lebsock, M. D., and T. S. L'Ecuyer, 2011: The retrieval of warm rain from CloudSat. *J. Geophys. Res.,* **116,** D20209

Lilly, D. K., 1968: Models of cloud-topped mixed layers under a strong inversion. *Q.J.R. Meteorol. Soc.*, **94**, 292–309.

Lin, W., M. Zhang, and J. Wu., 2009: Simulation of low clouds from the CAM and the regional WRF with multiple nested resolutions. *Geophys. Res. Lett.*, **36**:8.

Liu, Z., and Coauthors, 2009: The CALIPSO Lidar Cloud and Aerosol Discrimination: Version 2 algorithm and initial assessment of performance. *J. Atmos. Oceanic Technol.*, **26**, 1198–1213.

Luo, Z., G. Y. Liu, G. L. Stephens, and R. H. Johnson, 2009: Terminal versus transient cumulus congestus: A CloudSat perspective, *Geophys. Res. Lett.*, **36**, L05808.

Ma, C. C., C. R. Mechoso, A. W. Robertson, and A. Arakawa, 1996: Peruvian stratus clouds and the tropical pacific circulation: A coupled ocean-atmosphere GCM study, *J. Climate*, **9**, 1635–1645.

Mace, G. G., R. Marchand, Q. Zhang, and G. Stephens, 2007: Global hydrometeor occurrence as observed by CloudSat: Initial observations from summer 2006, *Geophys. Res. Lett*., **34**, L09808, doi:10.1029/2006GL029017.

Mace, G. G., Q. Zhang, M. Vaughan, R. Marchand, G. Stephens, C. Trepte, and D. Winker, 2009: A description of hydrometeor layer occurrence statistics derived from the first year of merged CloudSat and CALIPSO data, *J. Geophys. Res*., **114**, D00A26, doi:10.1029/2007JD009755.

Mansbach, D. K., and J. R. Norris, 2007: Low-level cloud variability over the equatorial cold tongue in observations and models. *J. Climate*, **20**, 1555–1570.

Marchand, R., G. G. Mace, T. Ackerman, and G. Stephens, 2008: Hydrometeor detection using CloudSat—An Earth-orbiting 94-GHz cloud radar. *J. Atmos. Oceanic Technol.*, **25**, 519–533.

Marks, C. J., and C. D. Rodgers, 1993: A retrieval method for atmospheric composition from limb emission measurements, *J. Geophys. Res*., **98**, 14939–14953, doi:10.1029/93JD01195.

Marra A.C., G.P. Marra, and F. Prodi, 2013: Numerical scattering simulations for interpreting simultaneous observations of clouds by a W-band spaceborne and a C-band ground radar. *European Journal of Remote Sensing*, **46**: 909-927, doi: http://dx.doi.org/10.5721/EuJRS20134654.

McGill, M. J., M. A. Vaughan, C. R. Trepte, W. D. Hart, D. L. Hlavka, D. M. Winker, and R. Kuehn, 2007:Airborne validation of spatial properties measured by the CALIPSO lidar, *J. Geophys. Res.*,**112**, D20201, doi:10.1029/2007JD008768.

Miller, M. A., M. P. Jensen, and E. E. Clothiaux, 1998: Diurnal cloud and thermodynamic variations in the stratocumulus transition, doi: http://dx.doi.org/10.1175/1520-0469(1998)055

Mitrescu, C., T. L'Ecuyer, J. Haynes, S. Miller, and J. Turk, 2010: CloudSat precipitation profiling algorithm—Model description. *J. Appl. Meteor. Climatol.*, **49**, 991–1003.

Moeng, C. H., S. H. Shen, and D. A. Randall, 1992: Physical processes within the nocturnal stratus-topped boundary layer. *J. Atmos. Sci.*, **49**, 2384–2401.

Morcrette, J.- J., and Y. Fouquart, 1985: On systematic errors in parametrized calculations of longwave radiation transfer. *Q.J.R. Meteorol. Soc.*, **111**: 691–708, doi: 10.1002/qj.49711146903

Moum, J., A. Perlin, J. Nash, and M. McPhaden, 2013: Seasonal sea surface cooling in the equatorial Pacific cold tongue controlled by ocean mixing, *Nature*, 5**00**,64–67, doi:10.1038/nature12363.

Muhlbauer, A., I. L. McCoy, and R. Wood, 2014: Climatology of stratocumulus cloud morphologies: microphysical properties and radiative effects. *Atmospheric Chemistry and Physics Discussions*, **14**, 6981-7023.

Nakajima, T. Y., K. Suzuki, and G. L. Stephens, 2010: Droplet growth in warm water clouds observed by the A-Train. Part I: Sensitivity analysis of the MODIS-derived cloud droplet sizes. *J. Atmos. Sci.*, **67**, 1884–1896.

Nicholls, S., 1984: The dynamics of stratocumulus: Aircraft observations and comparisons with a mixed layer model. *Q.J.R. Meteorol. Soc.*, **110**, 783–820.

Nicholls, S. and J. Leighton, 1986: An observational study of the structure of stratiform cloud sheets: Part I. Structure. *Q.J.R. Meteorol. Soc.*, **112**: 431–460, doi: 10.1002/qj.49711247209

Norris, J. R., Y. Zhang, and J. M. Wallace, 1998: Role of low clouds in summertime atmosphere-ocean interactions over the North pacific. *J. Climate*, **11**, 2482-2490.

Norris, J. R., and S. A. Klein, 2000: Low cloud type over the ocean from surface observations. Part III: Relationship to vertical motion and the regional surface synoptic environment. *J. Climate*, **13**, 245–256.

Petty, G. W., 1995: Frequencies and characteristics of global oceanic precipitation from shipboard present-weather reports. *Bull. Amer. Meteor. Soc.*, **76**, 1593–1616, doi: http://dx.doi.org/10.1175/1520-0477(1995)076<1593:FACOGO>2.0.CO;2

Polonsky, I., 2008: Level 2 cloud optical depth product process description and interface control document, report, 21 pp., CloudSat Proj., Colo. State Univ., Fort Collins.

Rahn, D. A., and R. D. Garreaud, 2011: Climatology of the 10-m wind along the west coast of South America from 30 years of high-resolution reanalysis. Segundo Congreso de Oceanografía Física, Meteorología y Clima, Coquimbo, Chile.

Rajeevan M, C.K. Unnikrishnan, and B. Preeth, 2012: Evaluation of the ENSEMBLES multi-model seasonal forecasts of Indian summer monsoon variability. *Clim Dyn,* **38**:2257–2274

Ramanathan, V., Cess, R. D., Harrison, E. F., Minnis, P., Barkstrom, B. R., Ahmad, E., and D. Hartmann, 1989: Cloud-radiative forcing and climate: Results from the Earth Radiation Budget Experiment. *Science*, **243**, 57-63.

Rapp, A.D., M. Lebsock, and T. L'Ecuyer, 2013: Low cloud precipitation climatology in the southeastern Pacific marine stratocumulus region using CloudSat. *Environ. Res. Lett.*, **8**, 014027.

Rapp, A.D., 2014: Cloud responses in the AMIP simulations of CMIP5 models in the southeastern Pacific marine subsidence region, *Int. J. Climatol., in press*.

Rasmussen, E. M., and J. M. Wallace, 1983: Meterological aspects of the E1 Niño Southern Oscillation. *Science*, **222**, 1195-1202.

Riehl, H., T. C. Yeh, J. S. Malkus, and N. E. Laseur, 1951: The northeast trade of the Pacific Ocean. *Q.J.R. Meteorol. Soc.*, **77**, 598–626, doi:10.1002/qj.49707733405

Richter, I., and C. R. Mechoso, 2004: Orographic influences on the annual cycle of Namibian stratocumulus clouds, *Geophys. Res. Lett*., **31**, L24108, doi:10.1029/2004GL020814.

Rogers, D. P., and D. Koračin, 1992: Radiative transfer and turbulence in the cloud-topped marine atmospheric boundary layer. *J. Atmos. Sci.*, **49**, 1473–1486, doi: http://dx.doi.org/10.1175/1520-0469(1992)049<1473:RTATIT>2.0.CO;2

Sandu, I., B. Stevens, and R. Pincus, 2010: On the transitions in marine boundary layer cloudiness, *Atmos. Chem. Phys*., **10**, 2377-2391,doi:10.5194/acp-10-2377-2010.

Schneider, S. H., 1972: Cloudiness as a global climatic feedback mechanism: The effects on the radiation balance and surface temperature of variations in cloudiness. *J. Atmos. Sci.*, **29**, 1413-1422.

Schumacher, C., and R. A. Houze Jr., 2000: Comparison of radar data from the TRMM satellite and Kwajalein oceanic validation site. *J. Appl. Meteorol.*, **39**, 2151–2164

Shao, Q., and D. A. Randall, 1996: Closed mesoscale cellular convection driven by cloud-top radiative cooling. *J. Atmos. Sci.*, **53**, 2144–2165.

Siebesma, A.P., and Coauthors, 2004: Cloud representation in general circulation models over the northern Pacific Ocean: A EUROCS intercomparison study. *Q.J.R. Meteorol. Soc., 130***,** 3245-3268.

Slingo, J. M., 1987: The development and verification of a cloud prediction scheme for the ECMWF model. *Q.J.R. Meteorol. Soc*., **113**: 899–927, doi: 10.1002/qj.49711347710

Soden, B. J., and I. M. Held, 2006: An assessment of climate feedbacks in coupled ocean–atmosphere models. *J. Climate*, **19**, 3354–3360.

Stephens, G., G. W. Paltridge and C. Platt, 1978: Radiation profiles in extended water clouds. III: Observations. *J. Atmos. Sci.*, **35**, 2133-2141.

Stephens, G. L., G. G. Campbell, and T. H. V. Haar (1981), Earth radiation budgets, J. Geophys. Res., 86(C10), 9739–9760, doi:10.1029/JC086iC10p09739.

Stephens, G.L., and Coauthors, 2002: The CloudSat mission and the A-Train: A new dimension of space-based observations of clouds and precipitation. *Bull. Amer. Meteorol. Soc.*, **83**, 1771-1790, doi:10.1175/BAMS-83-12-1771.

Stephens, G.L., 2005: Cloud feedbacks in the climate system: A critical review. J. *Climate*, **18**, 237-273.

Stephens, G.L and J. Haynes, 2007: Near global observations of the warm rain coalescence Process, *Geophys. Res. Lett.*, **34**, L20805.

Stephens, G. L., and Coauthors, 2008: CloudSat mission: Performance and early science after the first year of operation, *J. Geophys. Res*., **113**, D00A18, doi:10.1029/2008JD009982.

Stevens, B., W. Cotton, G. Feingold, and C. Moeng, 1998: Large-eddy simulations of strongly precipitating, shallow, stratocumulus-topped boundary layers. *J. Atmos. Sci.*, **55**, 3616–3638, doi: http://dx.doi.org/10.1175/1520-0469

Stevens, B., and Coauthors, 2003: Dynamics and chemistry of marine stratocumulus—DYCOMS II. *Bull. Amer. Meteor. Soc.*, **84**, 579–593.

Stevens, B., G. Vali, K. Comstock, R. Wood, M.C. Van Zanten, P. H. Austin, C. S. Bretherton, and D. H. Lenschow, 2005: Pockets of open cells and drizzle in marine stratocumulus. *Bull. Amer. Meteor. Soc.*, **86**, 51–57, doi: http://dx.doi.org/10.1175/BAMS-86-1-51

Stubenrauch. C. J., S. Cros. A. Guignard, and N. Lamquin, 2010: A six-year global cloud climatology from the atmospheric InfraRed sounder aboard the AQUA satellite: statistical analysis in synergy with CALIPSO and CloudSat. *Atmos. Chem. Phys.*, **10**, 7197-7214.

Su, H., and J. H. Jiang, 2013: Tropical clouds and circulation changes during the 2006/07 and 2009/10 El Niños. *J. Climate*, **26**, 399–413.

Szczodrak, M., P. H. Austin, P. B. Krummel, 2001: Variability of optical depth and effective radius in marine stratocumulus clouds. *J. Atmos. Sci.*, **58**, 2912–2926.

Tanelli, S., S. L. Durden, E. Im, K. S. Pak, D. Reinke, P. Partain, R. Marchand, and J. Haynes, 2008: CloudSat's cloud profiling radar after 2 years in orbit: performance, external calibration, and processing *IEEE Trans. Geosci. Remote Sens.*, **46,** 3560–73

Teixeira, J., and Coauthors, 2011: Tropical and subtropical cloud transitions in weather and climate prediction models: The GCSS/WGNE Pacific Cross-Section Intercomparison (GPCI), *J. Climate*, **24**, 5223–5256, doi: http://dx.doi.org/10.1175/2011JCLI3672.1

Turton, J. D. and S. Nicholls, 1987: A study of the diurnal variation of stratocumulus using a multiple mixed layer model. *Q.J.R. Meteorol. Soc.*, **113**: 969–1009, doi: 10.1002/qj.49711347712

Vali, G., R. D. Kelly, J. French, H. S. D. Leon, A. McIntosh, and R.E. Pazmany, 1998: Finescale structure and microphysics of coastal stratus. *J. Atmos. Sci.*, **55**, 3540–3564.

Van der Dussen, J.J., and Coauthors, 2013: The GASS/EUCLIPSE model intercomparison of the stratocumulus transition as observed during ASTEX: LES results. *J. Adv. Model. Earth Syst.*, **5**, 483-499, doi:10.1002/10.1002/jame.20033.

VanZanten, M. C., and B. Stevens, 2005: Observations of the structure of heavily precipitating marine stratocumulus *J. Atmos. Sci.*, **62**, 4327–4342, doi: http://dx.doi.org/10.1175/JAS3611.1

Vaughan, M. A., and Coauthors, 2009: Fully automated detection of cloud and aerosol layers in the CALIPSO lidar measurements. *J. Atmos. Oceanic Technol.*, **26**, 2034–2050.

Wallace, J.M., T.P. Mitchell, and C. Deser, 1989: The influence of sea surface temperature on surface wind in the eastern equatorial Pacific: seasonal and interannual variability. *J. Climate*, **2**, 1492-1499.

Wang, Q., and D. H. Lenschow, 1995: An observational study of the role of penetrating cumulus in a Marine Stratocumulus-Topped Boundary Layer. *J. Atmos. Sci.*, **52**, 2778–2787, doi: http://dx.doi.org/10.1175/1520-0469(1995)052<2778:AOSOTR>2.0.CO;2

Webb M.J., and Coauthors, 2006: On the contribution of local feedback mechanisms to the range of climate sensitivity in two GCM ensembles. *Clim Dyn.*, **27,**17–38.

Wilheit, T. T., 1986: Some comments on passive microwave measurement of rain. *Bull. Amer. Meteor. Soc.*, **67**, 1226–1232.

Winker, D. M., J. Pelon, and M.P. McCormick, 2003: The CALIPSO mission: spaceborne LiDAR for observation of aerosols and clouds *Proc. SPIE Int. Soc. Opt. Eng.*, **4893,** 1–11

Winker, D. M., W.H. Hunt, and M.J. McGill, 2007: Initial performance assessment of CALIOP. *Geophys Res Lett.*, **34**:L19803, doi: 10.1029/2007GL030135.

Wittenberg, A. T., A. Rosati, N.-C. Lau, J. J. Ploshay, 2006: GFDL's CM2 global coupled climate models. Part III: Tropical pacific climate and ENSO. *J. Climate*, **19**, 698–722, doi: http://dx.doi.org/10.1175/JCLI3631.1

Wood, R. and J. P. Taylor, 2001: Liquid water path variability in unbroken marine stratocumulus cloud. *Q.J.R. Meteorol. Soc.*, **127**: 2635–2662, doi: 10.1002/qj.49712757807

Wood, R., and D. L. Hartmann, 2006: Spatial variability of liquid water path in marine low cloud: The Importance of Mesoscale Cellular Convection. *J. Climate*, **19**, 1748–1764, doi: http://dx.doi.org.libezproxy.tamu.edu:2048/10.1175/JCLI3702.1

Wood, N., 2008: Level 2B radar-visible optical depth cloud water content (2B-CWC-RVOD) process description document. Colorado State University, 26 pp.

Wood, R. and Coauthors, 2011: The VAMOS ocean-cloud-atmosphere-land study regional experiment (VOCALS-REx): goals, platforms, and field operations *Atmos. Chem. Phys.* **11** 627–54

Wood, R., 2012: Stratocumulus clouds. *Mon. Wea. Rev.,* **140,** 2373-2423, doi: http://dx.doi.org/10.1175/MWR-D-11-00121.1

Wyant, M. C., C. S. Bretherton, H. A. Rand, and D. E. Stevens, 1997: Numerical simulations and a conceptual model of the stratocumulus to trade cumulus transition. *J. Atmos. Sci.*, **54**, 168–192, doi: http://dx.doi.org.lib-ezproxy.tamu.edu:2048/10.1175/1520 0469(1997)054<0168:NSAACM>2.0.CO;2

Xu, H., Y. Wang, and S.-P. Xie, 2004: Effects of the Andes on eastern Pacific climate: A regional atmospheric model study. *J. Climate*, **17**, 589–602, doi: http://dx.doi.org.lib-ezproxy.tamu.edu:2048/10.1175/1520-0442(2004)017<0589:EOTAOE>2.0.CO;2

Yue, J., L. Hoffmann, and M. Joan Alexander, 2013: Simultaneous observations of convective gravity waves from a ground-based airglow imager and the AIRS satellite experiment, *J. Geophys. Res. Atmos*., **118**, 3178–3191, doi:10.1002/jgrd.50341

Zhang, M.H., and Coauthors. 2005. Comparing clouds and their seasonal variations in 10 atmospheric general circulation models with satellite measurements. *J. Geophys. Res.,* **110**, D15S02,doi:10.1029/2004JD005021.